

# Dynamics, wakes, and regime transitions of a fixed angular particle in an unbounded inertial flow. II. From tetrahedron to sphere

Guodong Gai

*Department of Mathematics, University of British Columbia, Vancouver, BC, Canada*

Anthony Wachs \*

*Department of Mathematics, University of British Columbia, Vancouver, BC, Canada  
and Department of Chemical & Biological Engineering,  
University of British Columbia, Vancouver, BC, Canada*



(Received 8 March 2023; accepted 24 May 2023; published 27 June 2023)

In this study, we investigate an unbounded Newtonian fluid flow past a stationary Platonic polyhedron. To reveal the effects of the particle angularity and angular position on the flow regime transitions, we select the three following different angular positions of the Platonic polyhedrons: a face facing the flow (F), an edge facing the flow (E), and a vertex facing the flow (V). We consider all five Platonic polyhedrons whose sphericity increases with the number of faces and a sphere as an asymptotic polyhedron of sphericity 1 featuring an infinite number of faces. Two well-known regime transitions are studied as a function of the particle sphericity, the particle angular position and the particle Reynolds number  $Re$ : the loss of symmetry in the particle wake region and the loss of stationarity of the flow. In the multiplanar symmetry regime, the flow symmetry in the particle wake region is highly related to the particle front surface. The number and orientation of particle front surface edges determine the wake vorticity pattern. With increasing  $Re$ , the steady flow past an angular particle transitions to a planar symmetry regime for all particle shapes and all particle angular positions. The plane of symmetry in the planar symmetry regime selects one of the axis in the multiplanar symmetry regime, and its direction may change in time and/or with  $Re$ . In the unsteady regime, we notice a wide variety of periodic hairpin vortex shedding modes. These vortex shedding modes are determined by the shape of the flow recirculation region, which itself is a reflection of the angularity and the angular position of the particle. Furthermore, we present an in-depth analysis of the hydrodynamic forces exerted on the Platonic polyhedrons at the vertex angular position (V) for a wide range of Reynolds numbers  $100 \leq Re \leq 500$ . We attempt to understand and explain the significant variations in the flow regime transitions brought by the particle angularity and the particle angular position.

DOI: [10.1103/PhysRevFluids.8.064305](https://doi.org/10.1103/PhysRevFluids.8.064305)

## I. INTRODUCTION

The generic problem of inertial flows past a three-dimensional bluff body has been investigated for decades due to its omnipresence in engineering applications and human activities such as particulate air pollution, river sedimentation, and ocean dynamics [1–4]. The dynamics and path instability of particles such as solid spheres [5], cubes [6,7], oblique bodies [8], disks [9,10], or

---

\*wachs@math.ubc.ca

spheroidal bubbles [11] have been a focus of many recent researches. For freely moving particles in a carrier fluid phase, the dynamics of one phase affect the other in various ways, leading to complicated two-way interactions and complex flow dynamics that are difficult to decouple. In some engineering applications, such as steady underwater vehicles in constant current, or freely moving particles in a vertical path, the ideal scenario of steady flow past a fixed particle can be representative. For a fixed particle in a flow, which is the focus of this study, two main features are considered in the flow-particle interaction: (i) the regime transition and vortex structures in the particle wake region and (ii) the hydrodynamic forces exerted on the particle by the surrounding fluid, such as the drag force and the lift force. The understanding of these two features is beneficial to better comprehend the overall complex behavior of particle-flow interactions in both the fixed particle and freely moving particle cases.

Many previous studies focus on the basic configuration of a Newtonian flow past an isolated sphere, considering its omnidirectional symmetry [12–15]. In 1961, the regime transition mechanisms were observed and discussed by Magarvey *et al.* [16] using dye visualization experiments of a flow past a sphere. Johnson and Patel [17] proposed a thorough analysis of the dynamics of the laminar flow past a fixed sphere. A symmetry-breaking process was proposed and the unsteady vortex shedding dynamics are discussed. One hairpin vortex structure detached from the sphere rear region, followed by another hairpin structure induced by the interaction between the near-wake flow and the outer flow. This process repeats and a sequence of two-sided alternative hairpin vortex shedding occurs in a constant-oriented plane.

Particles other than a sphere would experience different cross-sectional forces depending on their angular position with respect to the incoming flow. To elucidate the effects of the particle shape and angularity on the flow regimes, several researchers studied the flow past a fixed/moving angular particle such as a cube or a tetrahedron, at low and intermediate Reynolds numbers [18–21]. In soil, rock mining engineering, and powder metallurgy applications, polyhedral solids are frequently encountered. For example, cubic particles can be used as catalysts, absorbents, and ferrofluids in the form of meta colloids [22]. A careful investigation of a laminar flow past a fixed cube was carried out by Saha *et al.* [18,23] for a low and moderate Reynolds number  $20 \leq \text{Re}_{\text{edge}} \leq 300$ , where  $\text{Re}_{\text{edge}}$  is the Reynolds number defined using the edge length of the cube. For the flow regimes studied, the drag coefficient was found to decrease with  $\text{Re}_{\text{edge}}$ , whereas one component of the lift coefficient rose in the planar symmetry regime. Klotz *et al.* [24] investigated experimentally the wake region behind a cube with a face facing the flow for moderate Reynolds numbers  $100 \leq \text{Re}_{\text{edge}} \leq 400$ . Two flow bifurcation mechanisms were confirmed and the vorticity in the wake region was reported to originate from corners of the bluff body for the flow regimes studied. This conclusion can be generalized to other angular particles, that the corner-induced vorticity (edge-induced vorticity in our study [25]) is important for the characterization of the particle wake flow regimes. Recently, Meng *et al.* [26] performed a series of highly resolved body-fitting numerical simulations of flows at small and moderate Reynolds numbers  $1 \leq \text{Re}_{\text{edge}} \leq 400$ . To reveal the flow regime transition mechanisms, various physical properties in the wake region of a fixed isolated cube, such as the streamlines, the vorticity pattern and the vortex-shedding frequency, were discussed. Four different regimes were identified: the orthogonal symmetry-steady (OSS), planar symmetry-steady (PSS), hairpin-vortex shedding (HS), and chaotic vortex shedding (CS) flow regime. Compared to the flow past a sphere, the sharp edges of the angular particles can lead to a different class of flow regimes. We shall see that most flow features in both steady and unsteady regime are dependent on the particle geometric shape, especially the edges on the particle front surface.

Flows past a cube undergo two supercritical bifurcations with increasing  $\text{Re}$ : (i) the first regular pitchfork bifurcation where the flow transitions from the orthogonal symmetric regime to the planar symmetry regime and (ii) the Hopf bifurcation where the flow becomes unsteady with hairpin vortices shed in the particle wake region [24]. The hairpin vortex shedding is reported to retain the planar symmetry with respect to a fixed plane. Then with increasing  $\text{Re}$ , the planar symmetry breaks and the vortex shedding begins to become chaotic [18]. The Landau's amplitude equation [27] was used to accurately determine the critical Reynolds numbers for the two supercritical bifurcations

[24,26]. Apart from the sphere and cube, several investigations were carried out on the inertial flows past a nonspherical bluff body such as a cylinder [7,28–30] and an ellipsoid [31–33].

In addition to the flow dynamics in the particle wake region, various correlations of the drag coefficient  $C_d$  have been established from numerical and experimental data to address the needs of industrial and engineering applications [34]. Based on a large database of experimental measurements [35], Haider and Levenspiel [36] established a correlation of the drag coefficient for nonspherical particles as a function of the sphericity and the Reynolds number, which is still widely used today in academic research as well as in engineering activities. The drag coefficient data used to draw this correlation, however, were obtained from freely settling particle experiments. The particles adopt time-dependent angular positions in the flow during the free settling/rising process. Even though it agrees well with experimental data, this correlation using only sphericity as a parameter fails to account for the particle angular position, which has been shown to have important effects on the fluid flow [37–39]. In 2008, Holzer *et al.* [40,41] obtained another correlation based on experimental data for the drag coefficient of various nonspherical particles using both the crosswise and lengthwise sphericity to account for the particle angular position [35,42]. This correlation was reported to have good accuracy for general nonspherical particles, but the correlation of Haider *et al.* [36] seems to be more accurate for isometric angular particles.

Richter *et al.* performed body-fitting numerical simulations of a fixed cube with various attack angles in laminar flows and proposed a correlation for the drag coefficient  $C_d$  [32,39]. The significant influence of the attack angle on the flow has been elucidated and emphasized. However, these studies only focused on a single particle shape, the cube, and considered a narrow range of Reynolds numbers. In Part I of this work [43], we investigated the unbounded flow past a fixed isolated regular tetrahedron (the most angular Platonic polyhedron) at the same three angular positions as those considered in the present work: edge facing the flow (TE), face facing the flow (TF), and vertex facing the flow (TV). A new symmetric double-hairpin vortex shedding (DHS) regime was noted in the TE case due to its unique angular position that features orthogonal symmetry. The formation of the double-hairpin vortices was considered to result from the *U-shape* recirculation region in the particle wake. We showed that the regime transition and vortex structures for the flow past a tetrahedron are highly dependent on its angular position.

Regardless of the existing large body of knowledge on particle-laden flows, the effects of the particle angularity on the flow regime transitions still remain unclear. A sound understanding of the flow past a fixed angular particle is pivotal to future studies of freely moving angular particles which are of vital importance in meteorology and sedimentology [44]. The current study uses a high-fidelity finite volume fictitious domain method implemented on a Cartesian adaptive octree grid to investigate the flow past a Platonic polyhedron in the range of Reynolds number  $100 \leq \text{Re} \leq 500$ . The Platonic polyhedrons are five isometric convex polyhedrons with an increasing number of polygonal faces, which are ideal candidates to describe the transition from highly angular particles to a smooth sphere [45,46]. For all Platonic polyhedrons, we observe the vorticity symmetry breakup, rich vortex structures and various new vortex shedding modes and provide a thorough analysis of the exerted hydrodynamic forces at the vertex facing the flow angular position (V).

The following is how this paper is organized: Sec. II gives the numerical method and dimensionless numbers involved in the current study; Sec. III describes the numerical setup, boundary conditions as well as geometric features of Platonic polyhedrons at the three angular positions; The validation of the numerical method and the choices of simulation parameters are presented in Sec. IV; Sec. V elucidates the effects of particle angularity on the fluid velocity and vorticity distribution and consequently on the flow regime transitions. We analyze the multiplanar symmetry regime, the planar symmetry regime, the periodic vortex shedding regime and the chaotic vortex shedding regime. A comprehensive discussion is given on the exerted hydrodynamic forces and vortex shedding frequency for all Platonic polyhedrons at the V position; Finally, we draw conclusions and perspectives for future work in Sec. VI.

## II. NUMERICAL METHOD AND DIMENSIONLESS NUMBERS

The distributed Lagrange multiplier/fictitious domain (DLM/FD) method describes a rigid body immersed in a fluid by representing its space with a *fictitious* fluid domain  $P$  that is enforced to behave as a rigid body. In the following, we use an asterisk  $*$  for dimensional quantities. Considering a cubic computational domain  $\Omega$  with boundary  $\Gamma$ , a solid subdomain  $P$ , i.e., an obstacle is dispersed in a Newtonian fluid of constant density  $\rho_f^*$  and viscosity  $\mu_f^*$ . The fluid subdomain is denoted as  $\Omega \setminus P$  to keep the liquid and solid strictly separated ( $\Omega \setminus P \cap P = \emptyset$ ). In many previous works, the main features of the DLM/FD method employed in this paper have been comprehensively presented [47–51]. For the sake of brevity, we only recall the governing equations for the fluid motion and the *combined equation of motion* for the particle-fluid mixture.

### A. Distributed Lagrange multiplier/fictitious domain (DLM/FD) method

The incompressible flow of a Newtonian fluid satisfies the following conservation of momentum and mass:

$$\rho_f^* \left( \frac{\partial \mathbf{u}^*}{\partial t^*} + \mathbf{u}^* \cdot \nabla \mathbf{u}^* \right) = -\nabla p^* + \mu_f^* \Delta \mathbf{u}^* \quad \text{in } \Omega \setminus P \quad (1)$$

$$\nabla \cdot \mathbf{u}^* = 0 \quad \text{in } \Omega \setminus P, \quad (2)$$

where  $\mathbf{u}^*$  denotes the fluid velocity vector and  $p^*$  the pressure;  $\Omega$  is the computational domain and  $P$  denotes the rigid particle.

The DLM/FD method relies on deriving an equation of motion for the fluid-particle mixture by combining the weak formulation of the fluid motion equation and that of the rigid particle. First, the weak formulation for the fluid subdomain  $\Omega \setminus P$  is obtained by imposing the rigid-body motion constraint (here the particle is stationary) on the particle surface  $\partial P$ . Then by imposing the rigid-body motion constraint in the whole particle subdomain  $P$ , the formulation is extended to the computational domain  $\Omega$  and corresponds to the so-called *combined equation of motion*. Finally, Lagrange multipliers  $\lambda^*$  are used to relax the rigid-body motion constraint in the particle subdomain  $P$ . Denoting  $\mathcal{W}_\Gamma$ ,  $\mathcal{W}_0$ ,  $\mathcal{L}_0$ , and  $\Lambda$  functional spaces of the solution satisfying boundary conditions [51], we solve in the case of a single stationary particle  $P$  in the following constrained problem: find  $\mathbf{u}^* \in \mathcal{W}_\Gamma$ ,  $p^* \in \mathcal{L}_0^2$  and  $\lambda^* \in \Lambda$  such that:

(1) Combined equation of motion:

$$\int_{\Omega} \rho_f^* \left( \frac{\partial \mathbf{u}^*}{\partial t^*} + \mathbf{u}^* \cdot \nabla \mathbf{u}^* \right) \cdot \mathbf{v}^* dx - \int_{\Omega} p^* \nabla \cdot \mathbf{v}^* dx + \int_{\Omega} \mu_f^* \nabla \mathbf{u}^* : \nabla \mathbf{v}^* dx = - \int_P \lambda^* \cdot \mathbf{v}^* dx, \quad (3)$$

$$\int_P \boldsymbol{\alpha}^* \cdot \mathbf{u}^* dx = 0. \quad (4)$$

(2) Continuity equation:

$$\int_{\Omega} -q^* \nabla \cdot \mathbf{u}^* dx = 0, \quad (5)$$

for all  $\mathbf{v}^* \in \mathcal{W}_0$ ,  $q^* \in \mathcal{L}^2(\Omega)$ , and  $\boldsymbol{\alpha}^* \in \Lambda$ . Finally, we rewrite Eqs. (3)–(5) in a nonvariational form that is more amenable to a finite volume (or a finite difference) spatial discretization [50,51].

We adopt the numerical approach of Ref. [51] that implements the DLM/FD solver in the *open-source* code Basilisk [52]. Basilisk offers a flexible implementation of hierarchically refined Cartesian grids and multigrid solvers with remarkable convergence features to solve Poisson/Helmholtz-type problems [52], as well as a second-order accurate projection algorithm to solve Eqs. (1) and (2). In a more general problem involving freely moving particles, an additional granular subproblem is solved using our *in-house* Grains3D solver [53,54] owing to its ability to handle efficiently collisions between rigid particles of complex shape. The particle motion is not considered here but Grains3D is used to create and position the rigid particles in the flow domain.

Further information on the implementation and validation of the DLM/FD solver can be found in the prior works of our group [43,49–51].

### B. Dimensionless numbers

The current study involves the following essential dimensionless quantities: (i) the particle sphericity  $\phi$ , the particle Reynolds number  $\text{Re}$ , and the particle angular position as input parameters, and (ii) the drag coefficient  $C_d$ , the lift coefficient  $C_l$ , the dimensionless vorticity  $\omega$ , and the Strouhal number  $\text{St}$  as output parameters.

The particle sphericity  $\phi$  is a measure of how closely a particle shape matches a perfect sphere. It is defined as the ratio of the surface area of a sphere  $S_{\text{sph}}^*$  to the surface area  $S_p^*$  of an angular particle with the same volume:

$$\phi = \frac{S_{\text{sph}}^*}{S_p^*}. \quad (6)$$

The closer  $\phi$  is to 1, the closer the angular particle shape is to a sphere. In the following discussions, the sphere with the same volume as the investigated angular particle is named the *volume-equivalent sphere*.

The particle Reynolds number  $\text{Re}$  is defined as

$$\text{Re} = \frac{\rho_f^* U_0^* D_{\text{sph}}^*}{\mu_f^*}, \quad (7)$$

where  $D_{\text{sph}}^*$  denotes the diameter of the volume-equivalent sphere:

$$D_{\text{sph}}^* = \left( \frac{6}{\pi} V_{\text{Platonic}}^* \right)^{1/3}, \quad (8)$$

with  $V_{\text{Platonic}}^*$  the volume of the Platonic polyhedron. We would like to remind the readers that the particle Reynolds number  $\text{Re}$  defined here is different from the edge Reynolds number  $\text{Re}_{\text{edge}}$  used for the previous studies of flow past a fixed cube [23,26]. Since the edge length of Platonic polyhedrons with the same volume has different values, we choose the diameter of the volume-equivalent sphere  $D_{\text{sph}}^*$  as a characteristic length.

The drag coefficient is defined as

$$C_d = \frac{8F_x^*}{\rho_f^* U_0^{*,2} \pi D_{\text{sph}}^{*,2}}, \quad (9)$$

where  $F_x^*$  denotes the streamwise component of the hydrodynamic force  $\mathbf{F}^*$  exerted on the stationary particle defined as follows:

$$\mathbf{F}^* = \int_{\partial P} [-p^* \mathbf{I} + \mu_f^* (\nabla \mathbf{u}^* + \nabla \mathbf{u}^{*,T})] \cdot \hat{\mathbf{n}} dS = \int_P \boldsymbol{\lambda}^* dx, \quad (10)$$

where  $\hat{\mathbf{n}}$  denotes the outward-oriented unit normal vector to the particle surface  $\partial P$ . Please note that in the context of the DLM/FD method and for a stationary particle [55],  $\mathbf{F}^*$  is computed as the integral of the Lagrange multipliers over  $P$  in Eq. (10).

The particle lift coefficient  $C_l$  and its two components along  $y$  and  $z$  axis ( $C_{l,y}$  and  $C_{l,z}$ ) are defined similarly:

$$C_{l,y} = \frac{8F_y^*}{\rho_f^* U_0^{*,2} \pi D_{\text{sph}}^{*,2}}, \quad C_{l,z} = \frac{8F_z^*}{\rho_f^* U_0^{*,2} \pi D_{\text{sph}}^{*,2}}, \quad (11)$$

where  $F_y^*$  and  $F_z^*$  denote two components of the lift force. The magnitude of the lift force coefficient  $C_l$  is defined as

$$C_l = (C_{l,y}^2 + C_{l,z}^2)^{1/2}. \quad (12)$$

Three components of the dimensionless vorticity are defined as

$$\omega_x = \frac{\omega_x^* D_{\text{sph}}^*}{U_0^*}, \quad \omega_y = \frac{\omega_y^* D_{\text{sph}}^*}{U_0^*}, \quad \omega_z = \frac{\omega_z^* D_{\text{sph}}^*}{U_0^*}, \quad (13)$$

with  $\omega_x^*$  ( $\omega_y^*$ ,  $\omega_z^*$ ) the corresponding component of the vorticity in the  $x$  ( $y$ ,  $z$ ) direction.

The Strouhal number describes the flow oscillating mechanism in the wake region of the particle:

$$\text{St} = \frac{f_c^* D_{\text{sph}}^*}{U_0^*}, \quad (14)$$

where  $f_c^*$  denotes the dominant frequency of the vortex shedding. Note that the Strouhal number  $\text{St}$  is therefore the dimensionless frequency using  $U_0^*/D_{\text{sph}}^*$  as the characteristic frequency scale, i.e., the inverse of the advective timescale, to make  $f_c^*$  dimensionless.

### III. NUMERICAL SETUP

We consider a stationary rigid Platonic polyhedron in a large fluid cubic domain with an edge length  $L = L^*/D_{\text{sph}}^* = 40$ . A Newtonian fluid flows past the fixed Platonic polyhedron located at  $(x_p, y_p, z_p) = (10, 20, 20)$  at three different angular positions: an edge (E) facing the flow, a face (F) facing the flow, and a vertex (V) facing the inlet flow. We refer to the cubic computational domain boundaries (i.e., the cube faces) as left and right in the  $x$  direction, top and bottom in the  $y$  direction and front and behind in the  $z$  direction such that  $\Gamma = \text{left} \cup \text{right} \cup \text{top} \cup \text{bottom} \cup \text{front} \cup \text{behind}$ .  $\mathbf{u}$  satisfies homogeneous Neumann boundary conditions on the right boundary and Dirichlet boundary conditions on all the other boundaries as well as on the surface  $\partial P$  on the stationary particle (no-slip condition). Denoting  $U_0$  the inlet velocity, the complete set of boundary and initial conditions reads as follows:

$$\mathbf{u}(\mathbf{x}, t) = (U_0, 0, 0) \quad \text{on } \Gamma \setminus \text{right}, \quad (15)$$

$$\mathbf{u}(\mathbf{x}, t) = (0, 0, 0) \quad \text{on } \partial P, \quad (16)$$

$$\frac{\partial \mathbf{u}}{\partial x}(\mathbf{x}, t) = (0, 0, 0) \quad \text{on } \text{right}, \quad (17)$$

$$\mathbf{u}(\mathbf{x}, 0) = (U_0, 0, 0) \quad \text{in } \Omega \setminus P, \quad (18)$$

where  $\mathbf{x} = (x, y, z)$  is the position vector and  $U_0 = 1$ . We assign an arbitrary zero reference value to the pressure  $p$  at the right boundary. The numerical setup is illustrated in Fig 1.

In the Cartesian octree adaptive grid strategy implemented in Basilisk, a parent cubic cell is sliced into eight subcubes for local grid refinement [51,52]. At each time step, the Cartesian octree grid is dynamically adapted by refining the grid in regions of strong gradient variations of any field of interest and coarsening regions with weak gradient variations. Here our primary field of interest is the flow velocity. A phase indicator field (0 in the fluid and 1 in the solid) is also used to guarantee that the neighborhood of the particle surface is always at the finest grid resolution. Using both the velocity field and the phase indicator field, we ensure that the flow structures in both the boundary layer around the particle and the wake region are well captured. Between two successive levels, the cell size differs by exactly a factor of 2 in the hierarchical grid. The size of the smallest cell in the grid ought to be  $\Delta x = L/2^{n_l}$ , with  $n_l$  the maximal refinement level. Figure 2 depicts the locally refined octree grid around the vortex structures identified by the lambda-2 isosurface [56]  $\lambda_2 = -1$

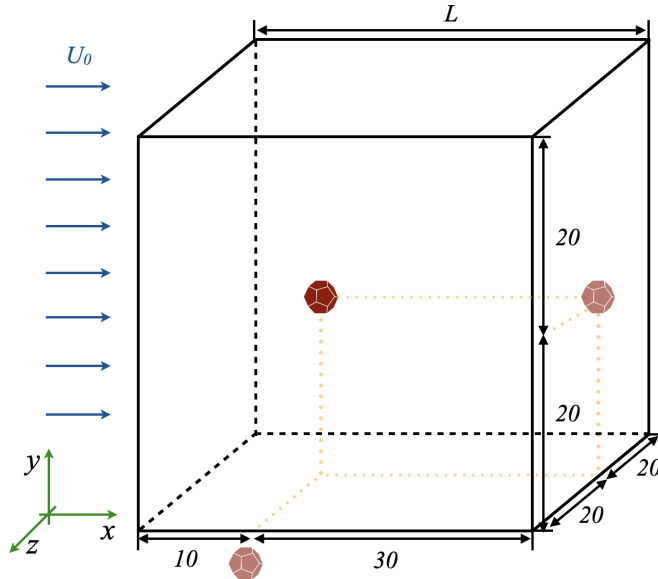


FIG. 1. Numerical setup: an inertial flow past a fixed Platonic polyhedron located in a cubic computational domain of side length  $L = 40$ , streamwise direction is  $x^+$ , i.e., fluid flows from left to right.

of the flow at Reynolds number  $Re = 500$  past a fixed cube in a vertex facing the flow position (CV).

We use a collocation point (CP) method [47,50,57] in the DLM/FD solver to impose the rigid-body motion constraints on the Platonic polyhedron at the discrete level on the grid. The complete set of points is the union of interior points chosen as grid nodes located inside the particle and surface Lagrangian points. The *parallel* point set is used to distribute Lagrangian points as uniformly as possible over the particle surface. In the *parallel* point set, surface points are located over lines parallel to the edges and this distribution technique has been shown to be efficient when applied to tetrahedrons and cubes [19,20,50] and can thus be extended to all Platonic polyhedrons [25]. Figure 3 illustrates the uniform distribution of the CP points on the surface of the five Platonic polyhedrons.

The surface of the tetrahedron (T, 4 faces), the octahedron (O, 8 faces), and the icosahedron (I, 20 faces) is made of equilateral triangles. The *parallel* point set therefore forms the vertices of

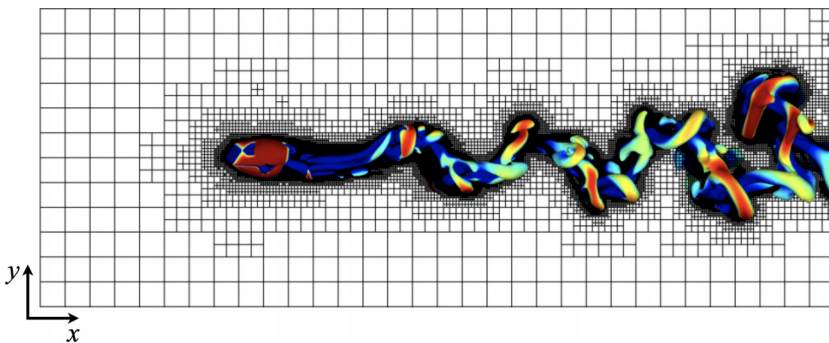


FIG. 2. Wake structures identified by the isosurface of  $\lambda_2 = -1$  and colored by  $u_x$  in the flow past the CV at  $Re = 500$  with adaptive grid in the  $x$ - $y$  plane at  $z = z_p$ .

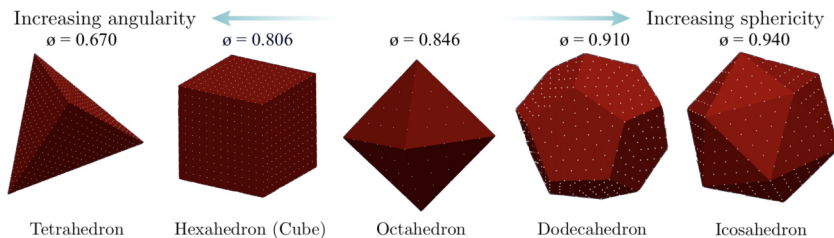


FIG. 3. Boundary points distribution on the surface of the Platonic polyhedrons.

a regular equilateral triangular mesh on each face of the particle. In contrast, the surface of the cube (C, 6 faces) and the dodecahedron (D, 12 faces) is made up of squares and regular pentagons, respectively. In the specific case of the dodecahedron (D), we add a point at the center of the regular pentagon and divide the pentagon into five (almost equilateral) triangles by connecting the center point to the face vertices. Subsequently, we distribute points on the center-vertex edges and inside each of the five (almost equilateral) triangles using the same method we use for the faces of the tetrahedron, the octahedron and the icosahedron.

With the adaptive grid refinement, we set the uniform surface-point-to-surface-point distance  $l_{pp}$  to  $2\Delta x$  and note that this is compatible with the size of the grid cells around the particle. Therefore, the number of particle surface points increases with the level of grid refinement  $n_l$ , providing a more accurate description of the particle and more reliable results on the hydrodynamic force computation.

Figure 4 presents the geometric features of the Platonic polyhedrons at the three angular positions: an edge (E), a face (F), and a vertex (V) facing the inlet flow. The front and side views of the five polyhedrons along the three coordinate axis ( $x$ ,  $y$ , and  $z$ ) are depicted. For the particles of high angularity such as the tetrahedron (T), the cube (C), and the octahedron (O), the front surface *seen* by the fluid flow changes dramatically with the angular position. With the increasing sphericity  $\phi$ , the number of faces on the particle surface increases and the crosswise cross-sectional surface area becomes closer to that of the volume-equivalent sphere, and this characterizes the dodecahedron (D) and the icosahedron (I). Hereafter, we use the *two-letter* abbreviation to describe a Platonic polyhedron at a specific angular position, for instance TE stands for a tetrahedron with an edge facing the flow angular position and IV stands for an icosahedron with a vertex facing the flow angular position.

The edge facing the flow angular position (E) is defined such that the two adjacent faces on the particle front surface remain symmetric with respect to the leading edge on the streamwise orthogonal projection in the  $y$ - $z$  plane. In the  $y$ - $z$  plane in Fig. 4, a single leading edge with two adjacent faces is noted in the TE, CE, and OE cases, whereas 5 (1 leading and 4 inclined) and 9 (1 leading and 8 inclined) edges are noted on the front surface if the DE and IE cases, respectively. The face facing the flow angular position (F) has a front face perpendicular to the streamwise  $x$  direction of the flow. For simplicity, we keep one edge on the leading face parallel to the  $y$  or  $z$  axis. The vertex facing the flow angular position (V) is such that a single particle vertex faces the flow. The center of mass and the opposite vertex are aligned, except for the tetrahedron where the rear face is orthogonal to the streamwise  $x$  direction. We see that three adjacent edges share the leading vertex on the front surface if the TV, CV, and DV cases, whereas we count four and five adjacent edges in the OV and IV cases, respectively.

The side views of the Platonic polyhedrons are illustrated in the fourth and fifth columns of Fig. 4. We observe that some shapes and angular positions break the orthogonal symmetry of the flow even in the low Reynolds number steady regime:

- (1) the two angular positions of the tetrahedron (TF, TV),
- (2) the vertex facing the flow cube (CV),
- (3) the face facing the flow octahedron (OF),

Particle	A.P.	$y-z$ view	$x-y$ view	$x-z$ view
Tetrahedron (T) $\phi = 0.670$	E			
	F			
	V			
Cube (C) $\phi = 0.806$	E			
	F			
	V			
Octahedron (O) $\phi = 0.846$	E			
	F			
	V			
Dodecahedron (D) $\phi = 0.910$	E			
	F			
	V			
Icosahedron (I) $\phi = 0.940$	E			
	F			
	V			

FIG. 4. Geometric features of the Platonic polyhedrons at the three angular positions (A.P.): E (edge), F (face), and V (vertex) with orthogonal projection in the  $y-z$ ,  $x-y$ , and  $x-z$  planes.

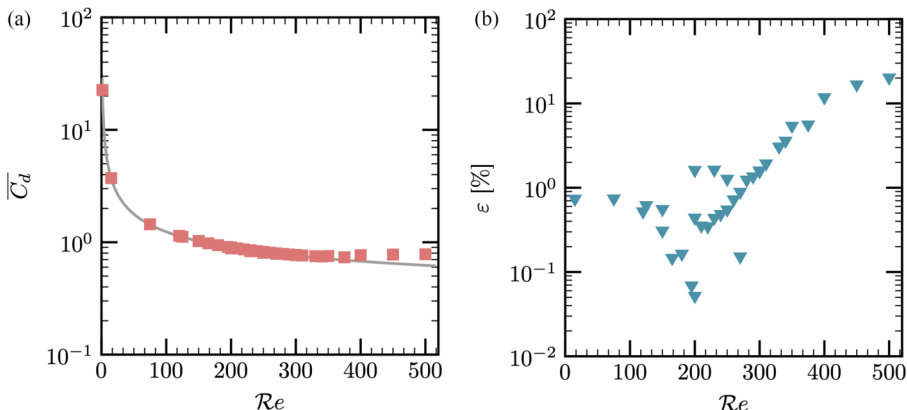


FIG. 5. (a)  $\overline{C_d}$  of the CV as a function of  $Re$  (■), comparison with Richter's correlation (—); (b) relative error  $\varepsilon$  between our computed results and the Richter's correlation for  $100 \leq Re \leq 500$  (▼).

- (4) the face facing the flow and vertex facing the flow dodecahedron (DF, DV),
- (5) the face facing the flow and vertex facing the flow icosahedron (IF, IV),

Consequently, at least one component of the lateral forces is nonzero in these cases, even when the flow regime is steady at a low  $Re$ . The magnitude of the lift coefficient  $C_l$  might still be pretty low, in particular in the case of polyhedrons with high sphericity such as the dodecahedron and the icosahedron. But it is important to stress that  $C_l$  is theoretically nonzero in the above cases due to the asymmetry of the angular position. Figure 4 serves as an excellent reference to help understand the occurring physical phenomena of the three-dimensional flow-particle interaction in different flow regimes.

#### IV. VALIDATIONS

To validate the DLM/FD solver, the effects of the domain size as well as the grid resolution on the convergence of the time-averaged drag coefficient  $\overline{C_d}$  are examined in our previous work [25]. Additionally, we perform a series of simulations of the flow past a fixed cube with a square face facing the flow (CF) at Reynolds numbers  $1 \leq Re \leq 500$ . We use the grid resolution ( $n_l = 12$ ,  $1/\Delta x = 102$ ), with  $n_l$  the maximal level of the grid refinement and  $1/\Delta x$  the number of smallest grid cells per volume-equivalent sphere diameter. As a reference, we consider the correlation established by Richter *et al.* [32], which provides the drag coefficient  $\overline{C_d}$  for the laminar flow past a fixed cube in the range  $10 \leq Re \leq 250$ .

Figure 5 gives the comparison between our numerical results and Richter's correlation. Figure 5(a) exhibits an excellent agreement ( $\varepsilon < 1\%$ ) between our numerical results and the reference correlation at  $10 \leq Re \leq 300$ . Higher relative errors ( $1\% < \varepsilon < 10\%$ ) are noticed for  $300 \leq Re \leq 500$  in Fig. 5(b). However, it is important to recall that Richter's correlation was established with data at  $10 \leq Re \leq 250$  and has never been tested outside this range of  $Re$ . We also observe that such a trend of  $\overline{C_d}(Re)$  with a minimum around  $Re \sim 300-350$  followed by a slight increase for larger  $Re$  and eventually a plateau agree well with computed results reported by Refs. [20,26] in the same flow configuration and experimental data reported by Ref. [36] in the case of a freely settling cube. Consequently, the relative errors with respect to Richter's correlation at  $Re > 250$  are deemed to be irrelevant and we safely use ( $n_l = 12$ ,  $1/\Delta x = 102$ ) for all computations in this work. The generated data set with such a spatial resolution is now physically analyzed in a reliable manner exempt from major biases stemming from spatial errors in the computations.

About time resolution, we choose the advective timescale  $t_{\text{ref}}^* = D_{\text{sph}}^*/U_0^*$  as the characteristic timescale. In all our simulations, the dimensionless time step  $\Delta t = \Delta t^*/t_{\text{ref}}^*$  is bounded by  $10^{-3}$  to

control the operator splitting error. Moreover, the Courant-Friedrich-Levy condition is satisfied to guarantee the numerical stability of the explicit treatment of the advection term in the momentum conservation equation. In the mathematical form, the time step  $\Delta t$  is dynamically updated at each discrete time by

$$\Delta t = \min \left\{ 10^{-3}, \min_m \frac{0.8 \Delta x_m^*}{|\mathbf{u}_{m^* \text{ref}}^*|} \right\}, \quad (19)$$

where  $m$  denotes an index spanning all grid cells.

Simulating over a long enough physical time guarantees that the flow regimes are fully established in our simulations. Most of our simulations run up to at least  $t = 400$  and several cases run up to  $t = 1500$ . Computing the flow over such long physical times enables us to perform a reliable statistical analysis of the time behavior of the flow in unsteady cases.

## V. RESULTS

To investigate the impact of the particle angularity and angular position on the flow dynamics and regime transitions in the particle wake region, we present a regime map as a function of Reynolds number  $Re$  and particle sphericity  $\phi$ . We classify the flow into four main regimes: multiplanar symmetry, planar symmetry, periodic vortex shedding, and chaotic vortex shedding, in increasing order of  $Re$ . We analyze the flow characteristics, including velocity, vorticity distribution, vortex structures, and drag/lift coefficients, for Platonic polyhedrons at the three angular positions in the range  $100 \leq Re \leq 500$ . This Reynolds number range encompasses the entire transition process from steady flows to chaotic flows in the particle wake, providing a comprehensive representation of the flow dynamics and the wake structures in these regimes.

### A. Reynolds number and flow regimes

Table I summarizes the regimes of flow past a Platonic polyhedron as a function of  $Re$ . Cases in the same regime are highlighted in the same color, with the upper and lower bounds in  $Re$ . The flow regimes identified and investigated in this study include:

- (1) Multiplanar steady symmetry regime (MSS) (■), in which the wake flow has symmetry around multiple planes;
- (2) Planar steady symmetry regime (PSS) (■), in which the wake flow has symmetry with respect to a single plane;
- (3) Periodic single-hairpin vortex shedding (HS) (■), in which the shedding of vortices is regular and periodic;
- (4) Chaotic vortex shedding (CS) (■), in which the shedding of vortices is irregular;
- (5) Double-hairpin vortex shedding (DHS) (■), a special HS in which two vortices are shed simultaneously from the particle (TE, more specifically).

The symmetry of the particle wake flow structures is an important factor to consider in the study of flow past an angular particle. At low  $Re$ , the flow field in the particle wake region exhibits multiplanar symmetry, with the number of planes depending on the number of edges on the particle's front surface. As  $Re$  increases, the flow transitions to a PSS regime, in which the plane of symmetry may rotate with time and  $Re$ . Prior to the chaotic shedding regime at large  $Re$ , the periodic shedding of hairpin vortices in the HS regime is typically observed. The TE case corresponds to a unique shape and a unique angular position that exhibits distinct behavior during the transition between regimes. In particular, the first transition is marked by the onset of the DHS regime immediately after the MSS regime. In the first stage (DHS-I,  $190 \leq Re \leq 330$ ), the double-hairpin shedding is *quasi* orthogonally symmetric, but eventually becomes planar symmetric. After the breakup of the planar symmetry, the hairpin vortex pairs are staggered but stay close to each other in the second stage (DHS-II,  $340 \leq Re \leq 360$ ). At  $Re = 370$ , the shedding becomes chaotic in the CS regime.

TABLE I. Regime transitions of the flow past a Platonic polyhedron at the three angular positions (A.P.): multiplanar symmetry (MSS, red), planar symmetry (PSS, green), periodic vortex shedding (PVS, orange), chaotic vortex shedding (CVS, blue), and double-hairpin vortex shedding (DHS, cyan); regime transition of the flow past a sphere: axisymmetric regime (ASR, pink).

Particle	A.P.	Regime I	Regime II	Regime III	Regime IV
<b>Tetrahedron (T)</b> $\phi = 0.67$	E	$100 \leq Re \leq 180$	$190 \leq Re^\dagger \leq 360$		$370 \leq Re \leq 500$
	F	$100 \leq Re \leq 120$	$130 \leq Re \leq 140$	$150 \leq Re \leq 230$	$240 \leq Re \leq 500$
	V	$100 \leq Re \leq 150$	$160 \leq Re \leq 180$	$190 \leq Re \leq 260$	$270 \leq Re \leq 500$
<b>Cube (C)</b> $\phi = 0.806$	E	$100 \leq Re \leq 130$	$140 \leq Re \leq 230$	$240 \leq Re \leq 330$	$340 \leq Re \leq 500$
	F	$100 \leq Re \leq 230$	$240 \leq Re \leq 300$	$310 \leq Re \leq 340$	$350 \leq Re \leq 500$
	V	$100 \leq Re \leq 120$	$130 \leq Re \leq 170$	$180 \leq Re \leq 260$	$270 \leq Re \leq 500$
<b>Octahedron (O)</b> $\phi = 0.846$	E	$100 \leq Re \leq 200$	$210 \leq Re \leq 260$	$270 \leq Re \leq 500$	
	F	$100 \leq Re \leq 240$	$250 \leq Re \leq 330$	$340 \leq Re \leq 500$	
	V	$100 \leq Re \leq 130$	$140 \leq Re \leq 160$	$170 \leq Re \leq 300$	$310 \leq Re \leq 500$
<b>Dodecahedron (D)</b> $\phi = 0.91$	E	$100 \leq Re \leq 190$	$200 \leq Re \leq 240$	$250 \leq Re \leq 420$	$430 \leq Re \leq 500$
	F	$100 \leq Re \leq 180$	$190 \leq Re \leq 220$	$230 \leq Re \leq 330$	$340 \leq Re \leq 500$
	V	$100 \leq Re \leq 180$	$190 \leq Re \leq 240$	$250 \leq Re \leq 360$	$370 \leq Re \leq 500$
<b>Icosahedron (I)</b> $\phi = 0.94$	E	$100 \leq Re \leq 190$	$200 \leq Re \leq 240$	$250 \leq Re \leq 340$	$350 \leq Re \leq 500$
	F	$100 \leq Re \leq 190$	$200 \leq Re \leq 240$	$250 \leq Re \leq 320$	$330 \leq Re \leq 500$
	V	$100 \leq Re \leq 200$	$210 \leq Re \leq 260$	$270 \leq Re \leq 330$	$340 \leq Re \leq 500$
<b>Sphere (S)</b> $\phi = 1.0$		$100 \leq Re \leq 210$	$220 \leq Re \leq 270$	$280 \leq Re \leq 350$	$360 \leq Re \leq 500$

<sup>†</sup>The DHS regime contains two sub-regimes: DHS-I ( $190 \leq Re \leq 330$ ) and DHS-II ( $340 \leq Re \leq 360$ ).

For particles with high angularity, such as tetrahedrons (T), cubes (C), and octahedrons (O), the critical Reynolds numbers  $Re_{cr}$  of flow transition vary more with angular position than those of particles with high sphericity (D, I). For example, the flow past the CE or the CV transitions from the MSS regime to the PSS regime at  $Re = 140$  and  $Re = 130$ , respectively, whereas, the first regime transition and the merging of the vorticity tubes in the CF case is only observed at  $Re = 230$ . The two leglike vortex tails identified by the  $\lambda_2$  criterion is observed in the CF case at  $Re = 250$ , even though the vorticity patterns in the particle wake region already show clear planar symmetry at  $Re = 240$ . Here we propose that the critical Reynolds number should lie between  $230 \leq Re_{cr, M \rightarrow P} \leq 240$  as shown in Table I since the vorticity pattern is a more sensitive indicator of the flow field symmetry than the  $\lambda_2$  pattern in the steady flow. With increasing sphericity (D, I), the particle has more faces and more closely resembles a sphere. The angular positions have less effects on the regime transitions. For example, the critical Reynolds numbers have similar values of about  $Re_{cr, M \rightarrow P} \approx 200$  for the transition from the MSS regime to the PSS regime of the flow past a dodecahedron (D) and an icosahedron (I) at any angular position. Similar results are also obtained for the critical  $Re_{cr, P \rightarrow H}$  from the PSS regime to the HS regime. However, from the PSS regime to the CS regime, the difference in the regime transition brought by the particle angular position is still noticeable. It is interesting to note that at the face angular position (F), the flow past the TF becomes chaotic at  $Re = 240$  while the flow past the OF remains in the HS regime up to at  $Re = 500$ . Above  $Re = 500$ , the flow past the OF will eventually become chaotic. Here, we keep our study within the range  $100 \leq Re \leq 500$ . We see that the particle sphericity  $\phi$  and angular position are both important factors of the flow regime transitions in the particle wake region.

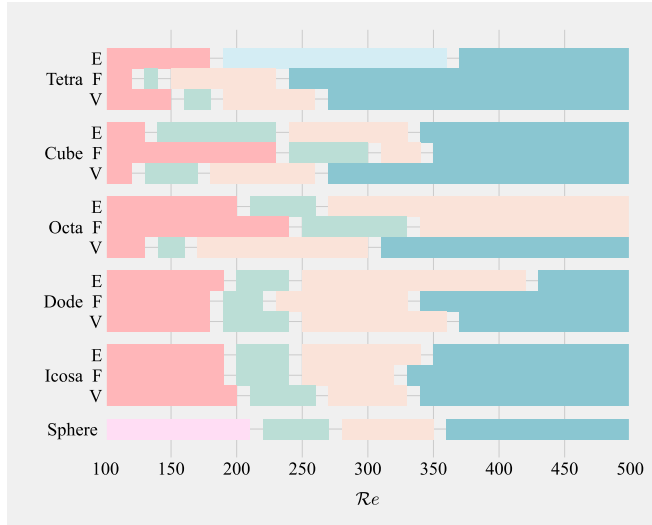


FIG. 6. Regime transition map of the flow past a Platonic polyhedron at the three angular positions (A.P.): multiplanar symmetry (red), planar symmetry (green), periodic vortex shedding (orange), chaotic vortex shedding (teal), and double-hairpin vortex shedding (light blue); regime transition of the flow past a sphere: axisymmetric regime (pink).

The regime transition of the flow past a fixed sphere is illustrated in Table I for reference. With the increase in the number of symmetry planes to infinity, we observe that the axisymmetric regime supersedes the MSS regime in the case of the sphere. Subsequently, the PSS, HS, and CS regimes remain in the same sequence as for the Platonic polyhedrons. Notably, the two critical Reynolds numbers,  $210 \leq Re_{cr,M \rightarrow P} \leq 220$  and  $270 \leq Re_{cr,P \rightarrow H} \leq 280$ , show close but slightly higher values compared to the three angular positions of the icosahedron.

Figure 6 illustrates the regime map of the flow past a Platonic polyhedron at the three angular positions (E, F, V) at  $100 \leq Re \leq 500$ . We employ the same color code as in Table I for the flow regimes. The range of  $Re$  for different flow regimes is represented by the length of the horizontal bar in Fig. 6, ensuring clear illustration and visual emphasis. As a result of the first regular bifurcation, the steady flow transitions from the MSS regime to the PSS regime. In Fig. 6, the MSS regime ends between  $Re = 130$  and  $Re = 200$  for most cases. The critical Reynolds numbers for regime transitions have higher values for particles with high sphericity (D, I), except for some exceptional cases such as the CF and the OF. Due to the second Hopf bifurcation, the flow regime changes from the PSS regime to the periodic hairpin vortex shedding (HS or DHS) regime. Usually, the PSS regime has a narrower range of  $Re$  compared to the DHS and HS regime. The angular position has a significant effect on the regime transitions of flow past a highly angular particle (T, C, O). In the OF case, the flow regime remains steady at  $Re = 330$ , while at  $Re = 170$ , the flow already transitions to the HS regime in the OV case. Similarly, the flow remains in the PSS regime at  $Re = 300$  in the CF case, whereas we see hairpin vortex shedding at  $Re = 180$  in the CV case. At  $Re = 350$ , the flow past the TE remains in the DHS regime, while the flow past an icosahedron (IE, IF, and IV), the most spherical Platonic polyhedron, has already become chaotic. The last regime transition from the HS/DHS regime to the CS regime is also strongly influenced by the particle angular position. The flow past the DE transitions to the CS regime at  $Re = 430$  while the dodecahedron (OE, OF) remains in the HS regime up to  $Re = 500$ . These angular positions display a significant stability in their vortex shedding structures, showcasing a critical  $Re_{cr,H \rightarrow C}$  that surpasses even that of the sphere. Despite the icosahedron having a high sphericity of  $\phi = 0.94$ , it cannot be considered equivalent to a sphere in terms of regime transition due to the noticeable differences in the  $Re_{cr}$  values. In the

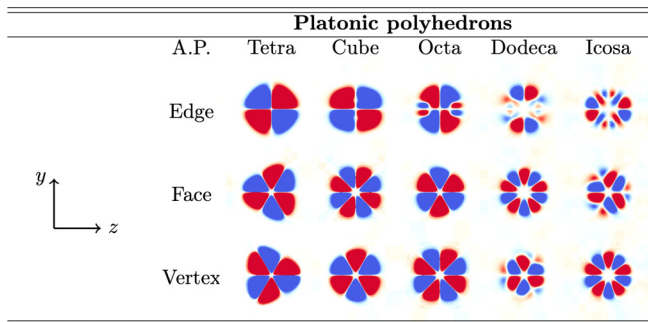


FIG. 7. Symmetry of the wake vortex structure identified by streamwise vorticity  $\omega_x$  (positive in red, negative in blue, and near-zero in white) of the flow in the MSS regime past a Platonic polyhedron in the  $y$ - $z$  plane located at  $x = x_p + 1.5$ .

following, we discuss the different flow regimes separately to gain a deeper understanding of the flow dynamics.

## B. Multiplanar symmetry regime

At low  $Re$  in the MSS regime, the flow remains steady and laminar as it passes around the particle. The vorticity distributions, as well as the flow velocity field in the near-wake and far-wake region, are all important factors in this steady regime.

### 1. Vorticity pattern and wake symmetry

At low  $Re$  in the MSS regime, when the fluid passes around the angular particle, a pair of opposite-signed vortices is generated on a front edge of the particle. It was observed in the experiments of Klotz *et al.* [24] for the flow past a fixed CF that four pairs of vortices were formed on the four front edges. Here we confirm this observation by high-fidelity numerical simulation results and notice that it can be generalized to all Platonic polyhedrons. For angular particles, the leading edges on the front surface disrupt the flow streamlines. These vortex pairs are transported downstream of the particle, featuring a tubelike shape in the  $\omega_x$  isosurfaces, preserving the information of the particle geometry. We summarize the streamwise vorticity  $\omega_x$  patterns in the wake region of the Platonic polyhedron at the three angular positions in Fig. 7. All the vorticity patterns exhibit multiple axes (in the  $y$ - $z$  plane, planes in 3D) of symmetry, which are determined by the geometry of the particle front surface. For example, the TF has three pairs of opposite-signed vortices, originating from the three leading edges on the front surface. The CF has four pairs of vortices and four axes of symmetry, which align with the four leading edges of the square front surface. In the edge angular position (E), the vorticity patterns show two pairs of opposite-signed vortices for all particle shapes, as there is only one single leading edge. The DE and the IE have more complex vortex structures, which arise from the secondary edges behind the leading edge on the particle front surface. In the vertex angular position (V), the leading edges are not perpendicular to the upcoming stream and the vortex pair is formed on both sides of the same edge. The number of axis of symmetry in the vorticity patterns equals the number of leading edges on the front surface of the particle. Although the TV and the TF have similar vorticity patterns in the wake region, the size of the vortex pairs produced by the TV is slightly smaller than that of the TF.

When two opposite-signed vortices of similar intensity approach each other, the mutual exclusion creates an equilibrium zone between them. At low  $Re$ , the equilibrium zone between the approaching vortices is wide enough to maintain stability in the vorticity pattern. The presence of multiplanar symmetry also results in a small or zero total lift force on the particle, depending on the particle shape and angular position.

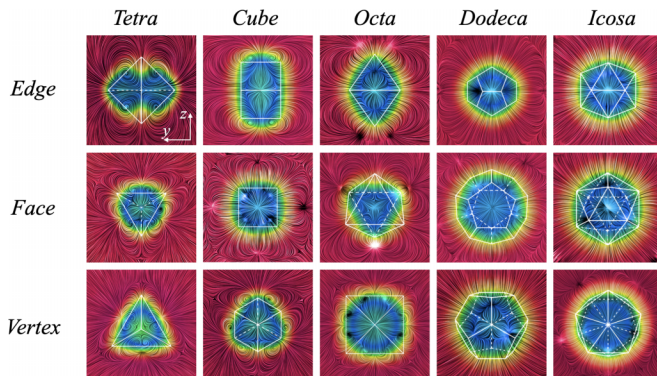


FIG. 8. LIC streamlines of the flow at  $Re = 100$  in the near-wake region of the Platonic polyhedron in the  $y$ - $z$  plane at  $x = x_p + 1$ . LIC streamlines are colored by the flow velocity magnitude (from min in dark blue to max in dark red) and particle edges are projected as white lines.

## 2. Near-wake structures

To more clearly illustrate the flow field in the MSS regime, we present the streamlines in line integral convolution (LIC) in the  $y$ - $z$  plane in the near-wake region of the Platonic polyhedron, as shown in Fig. 8. This visualization allows us to gain a deeper understanding of the flow symmetry in the wake region. LIC is a powerful tool for visualizing fluid velocity fields. Instead of adapting the start and end of streamlines to a specific velocity field, the LIC conveys all structural features of the flow such as velocity vector orientation, vortices, and in particular, the location of critical points. The color of the velocity field shows the flow velocity magnitude, from blue to red denoting the region with low to high velocity. The centers of the wake vortices locate at about one diameter downstream of the particle  $x = x_p + 1$ . It is clear that the multi-axis symmetry of the vorticity patterns depicted in Fig. 7 is closely related to the symmetry of the streamlines in Fig. 8.

The LIC clearly illustrates the presence of two pairs of opposite-signed vortices in the TE case in the  $y$ - $z$  plane. Comparing the TF and the TV, we see that three pairs of vortices are generated from the three leading edges of the TE. However, the vortex pairs are larger in size in the TF case compared to that in the TV case. The difference in the size of the vortex pairs is due to the fact that they are created by two different types of leading edges: perpendicular to the incoming flow (TF) or inclined but nonperpendicular to the streamwise  $x$  direction. Other Platonic polyhedrons, such as the CE, the CV and the OV, also exhibit similar structures. Particles of higher sphericity (D, I) tend to have a more complex front surface geometry and a larger number of leading edges, which makes it difficult to accurately depict the vortices behind the particle using streamlines. As a result, the vortex structures in the wake region of these particles may not be as clearly visible as those of more angular particles (such as T, C, and O). However, the symmetry axis of these higher sphericity particles are clearly depicted. For example, behind the IV, the streamlines preserve five axes of symmetry. The symmetry of the streamlines are aligned with the multi-axis symmetric vorticity pattern shown in Fig. 7.

The multiplanar (axis in the  $y$ - $z$  plane) symmetry of the wake structures is also influenced by the particle rear surface. Although the front and the rear surface of Platonic polyhedrons are not identical, they happen to have the same number of symmetry axis. If we modify the shape of the polyhedrons such that they are not regular, the vorticity pattern stretches and the flow regime transitions at a different  $Re$  from the regular Platonic polyhedrons. This is particularly true if we modify the rear surface by changing the location of one of its vertices. For instance, if we move the rear vertex of the TF toward the top edge by  $20\% D_{\text{sph}}^*$ , then the vorticity pattern changes to planar symmetry at  $Re = 100$ . With a smaller modification of the rear vertex (moving  $5\% D_{\text{sph}}^*$  closer to the top edge of TF), though, the vorticity pattern remains triaxis symmetric.

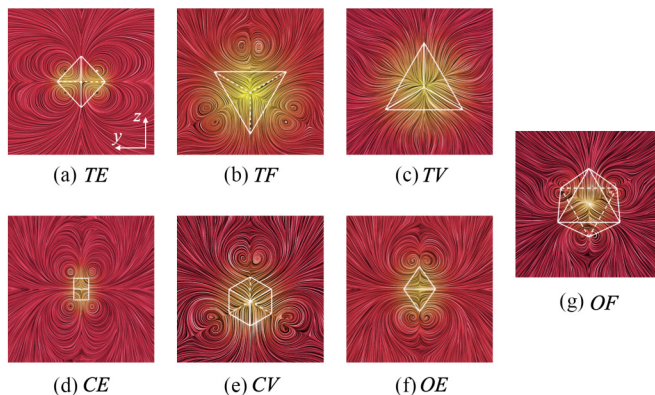


FIG. 9. LIC streamlines of the flow at  $\text{Re} = 100$  in the far-field region of the Platonic polyhedron in the  $y$ - $z$  plane at  $x = x_p + 10$ . LIC streamlines are colored by the flow velocity magnitude (from min in dark blue to max in dark red, same color map as in Fig. 8) and particle edges are projected as white lines.

### 3. Far-wake structures

In addition to the near-wake flow field, we also investigate the streamlines in the far-wake region in the MSS regime. It is worth noting that the effects of particle angularity are not limited to the near-wake region, as vortex structures are carried downstream up to 30 behind the particle. Figure 9 shows all the cases in which these far-wake vortices are observed, including all three angular positions of the tetrahedron TE/TF/TV, the CE and the CV, the OE and the OF. These far-wake vortices that are only observed for particles with high angularity (T, C, O), retain the same axis of symmetry as in the near-wake region of the particle. The existence of these far-wake vortices is due to the high intensity of the edge-induced vortices that allows them to penetrate the recirculation region and maintain their symmetry. The vorticity pattern in the  $y$ - $z$  plane fades progressively with the increasing distance from the particle wake. In contrast, for dodecahedra (D) and icosahedra (I), the vortex structures in LIC are no longer visible outside of the recirculation region. The presence of these far-wake vortices should be taken into account when simulating large numbers of angular particles, as they have significant long-range effects.

## C. Symmetry breakup

### 1. Planar breakup mechanism

As  $\text{Re}$  increases, the multiplanar symmetry of the flow breaks down and becomes planar symmetric, as shown in Fig. 10. The streamwise component of the vorticity  $\omega_x$  is plotted in the  $y$ - $z$  plane on the lee side of the particle ( $x \approx x_p + 0.5$ ). This plane intersects most of the particles, except the TE, which results in a hollow region visible in the plots in Fig. 10. The distribution of  $\omega_x$  is shown for all Platonic polyhedrons at the three angular positions (E, F, V). The MSS regime is located at the top, while the PSS regime is presented at the bottom for comparison.

The symmetry breakup in the wake flow is caused by the change of the vorticity distribution on the particle rear surface. Let us take the example of the CF case (highlighted in the red box) in Fig. 10(b). Four pairs of opposite-signed vortices are generated from the four front edges of the CF. At low  $\text{Re}$ , the vortices are transported along the particle rear surface downstream to the wake region, maintaining their symmetry with respect to four axes. At the middle of the leading edge, an equilibrium region behaves like a wall separating the two opposite-signed vortices. As  $\text{Re}$  increases, the vortex cores become larger and this equilibrium can no longer hold. As a result, one corner-generated vortex extends an arm toward another vortex of the same sign generated by its neighbor corner. For example, the top right corner (blue, 1) extends a blue arm toward the top left corner

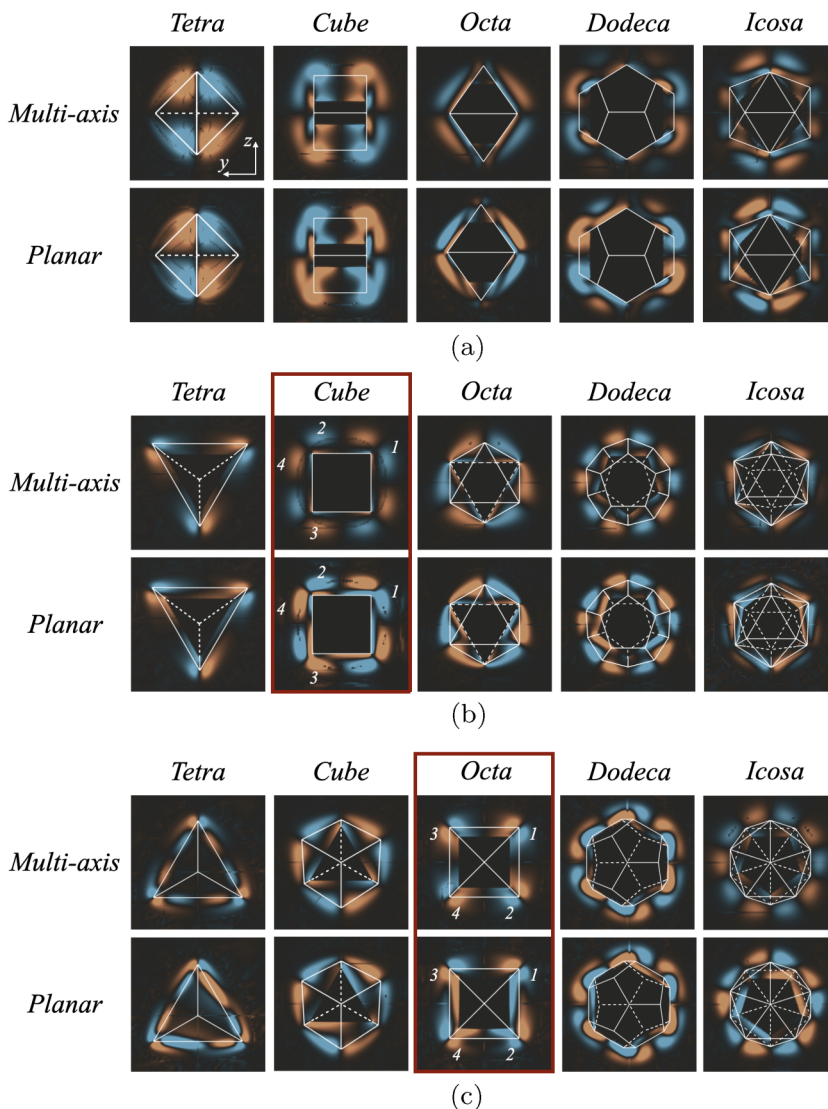


FIG. 10. Distribution of streamwise vorticity  $\omega_x$  (positive in orange, negative in blue, and near-zero in black) on the rear surface in the  $y$ - $z$  plane located at  $x \approx x_p + 0.5$  of the Platonic polyhedron at the three angular positions in the flow in the MSS regime and in the PSS regime. (a) Edge, (b) Face, and (c) Vertex.

(blue, 2). This vortex arm is attached to the rear surface due to the presence of an opposite-signed vortex, which is pushed slightly outward by the vortex arm. On the other side of the cube, a similar but opposite-signed vortex arm connects the bottom left vortex (orange, 3) and the top left vortex (orange, 4). Consequently, two larger vortices of opposite signs are formed on either side of the cube in the PSS regime, which are in equilibrium with each other and symmetric with respect to the cube diagonal. In Fig. 10(c), the OV case (highlighted in the red box) undergoes the same symmetry breakup process: the blue vortex 1 merges with the vortex 2 and the orange vortex 3 merges with vortex 4.

The mutual exclusion between opposite-signed vortices is the main reason for the emergence of symmetric vorticity patterns in the MSS regime. The equilibrium region between two opposite-

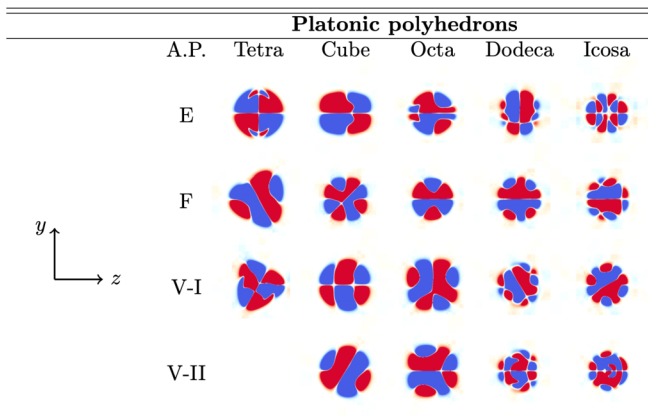


FIG. 11. Symmetry of the wake vortex structure identified by streamwise vorticity  $\omega_x$  (positive in red, negative in blue, and near-zero in white) of the flow in the PSS regime past a Platonic polyhedron in the  $y$ - $z$  plane located at  $x = x_p + 1.5$ .

signed vortices on the rear surface is wide enough to preserve the multiplanar symmetry. On the other hand, the mutual attraction of vortices of the same sign contributes to the emergence of the PSS regime. At a higher  $Re$ , the vortex core increases and the length of the vortex tubes grows. The mutual attraction of vortices of the same sign leads to the merging of vortex tubes, disrupting the multiplanar symmetry of the particle wake. The breakup of the multiplanar symmetry is mainly due to the merging and redistribution of the vortices. With two large opposite-signed vortices on the particle rear surface, where the pressure is relatively low and the streamlines are mainly deflected by the pressure gradient, the edge-induced vortices are stabilized at higher  $Re$  until the onset of the periodic vortex shedding. Please note that the vorticity distribution on the front surface of the particle remains multiplanar symmetric in the PSS regime. The same mechanism is also observed for other Platonic polyhedrons in Fig. 10, with the exception of the TE case. This particular shape at a special angular position is highly symmetric, such that the vortex shedding begins while maintaining the *quasiorthogonal* symmetry of the hairpin vortex structure in the DHS-I regime.

## 2. Planar symmetry regime

Figure 11 shows the vorticity patterns in the particle wake region in the PSS regime. Regardless of the number of symmetry axis the particle has in the MSS regime, the vorticity pattern collapses to a planar symmetry with respect to a single plane in the PSS regime. As previously mentioned, the presence of two large opposite-signed vortices in this regime enhances the stability of the vorticity distribution compared to the pattern in the MSS regime. In the edge angular position (E), the symmetry plane is either parallel or perpendicular to the leading edge. In the face angular position (F), after the transition to the PSS regime, the vortex structure randomly selects one of the symmetry axis of the MSS regime, as shown in Fig. 7. The symmetry plane in the CF case is oriented at  $45^\circ$  with respect to the  $x$ - $y$  plane. However, each of the four symmetry planes of CF in the MSS regime can be selected in the PSS regime. With a square cross-section, the OV presents the same planar symmetry pattern as that in the CF case.

We investigate the flow past a vertex Platonic polyhedron (V) with smaller increments of  $Re$ . In the case of CV, OV, DV, and IV, we reveal that there exist at least two possible directions of the symmetry plane that always contains the  $x$  axis, as shown in the last two rows (V-I and V-II) in Fig. 11. This confirms that the symmetry plane is *randomly* chosen from the symmetry planes in the MSS regime. There may also be a second direction of symmetry for the TV at a certain  $Re$  not

considered in this study. Upon further increasing  $Re$ , the symmetry plane becomes unstable and we observe a switch of direction at different times in the HS regime.

#### D. Periodic vortex shedding regime

##### 1. Periodic vortex shedding modes

We present the diverse vortex shedding modes in the HS/DHS regime in Fig. 12. The vortex structures are three-dimensional and presented in the view perpendicular to the  $x$ - $z$  plane on the left half and to the  $x$ - $y$  plane on the right half of Fig. 12. Please note that the flow is unsteady in the HS and DHS regimes. The vortex structures shown in Fig. 12 correspond to a snapshot at a time when the flow regime is established.

The vortex shedding mode and frequency in the particle wake are strongly dependent on the angular position. There is a distinct difference in the shedding modes of the tetrahedron in the three angular positions (E, F, V). A unique double-hairpin vortex shedding (DHS) mode manifests in the TE case, of which the formation mechanism and dynamics are discussed in our previous work [43]. Although the TF and the TV have similar shedding modes, the onset of the HS regime occurs at different critical Reynolds numbers  $Re_{cr}$ . The CE also exhibits a particular vortex shedding mode, in which a large bulky hairpin is accompanied by a small slim one, instead of a pair of similar-sized hairpin structures alternatively shed as seen in the CF and CV cases. The OE and the OF present vortex pairs that are smaller, more compact and shed at a higher frequency than that in the OV case. It is worth noting that the OE and the TE are the only two cases in which six periods of vortex shedding are visible in the distance of 30 downstream the particle, as depicted in Fig. 12. The CE and the OF have a slightly lower shedding frequency, with five periods visible in the snapshots. In contrast, the TF, TV, and OV cases manifest only three periods, half that in the OE and TE cases. It appears that the edge angular position (E) tends to have a higher shedding frequency compared to the other two angular positions (F, V) for particles such as the T, the C, and the O.

Particles with higher sphericity, such as the dodecahedron (D) and the icosahedron (I), have a similar shedding frequency (four periods in the snapshot) and exhibit vortex shedding modes analogous to that observed in the flow past a sphere. Additionally, the vortex shedding modes in the D and I cases remain akin among all three angular positions, except for the orientation of the vortex shedding plane. For instance, it is difficult to discern a difference in the hairpin vortices in the DV and IE cases in Fig. 12. The particle angular position has a minimal effect on the vortex structures and the shedding mode for these particles of high sphericity. Furthermore, we offer a supplementary perspective of the vortex structures via a side view, detailed in Appendix B.

##### 2. Flow velocity field

Figure 13 shows the snapshots of the streamlines in LIC in the periodic vortex shedding HS/DHS regime. The recirculation region in the particle wake has relatively low velocity and is highlighted in green-blue color in Fig. 13. All the Platonic polyhedrons exhibit a pair of vortices in both the  $x$ - $y$  plane and the  $x$ - $z$  plane. For most of the cases investigated (except for the TE), the recirculation region behind the Platonic polyhedron features an oval shape similar to that observed behind a sphere. The vortex shedding is characterized by the alternating detachment of hairpin structures from the recirculation region at different frequencies in a fixed or moving shedding plane. As observed in the wake region of a sphere, one vortex sucks the fluid from the surrounding bulk flow and the other opposite-signed vortex. As the volume of the vortex grows, the recirculation can no longer hold it in place and the vortex detaches from the particle wake region, flowing downstream. This process repeats as the opposite vortex then begins to grow and detach [58]. These vortices detach alternatively from the recirculation region in a predictable pattern, leading to the HS regime. The size of the vortices formed in the particle wake is limited by the volume of the recirculation region.

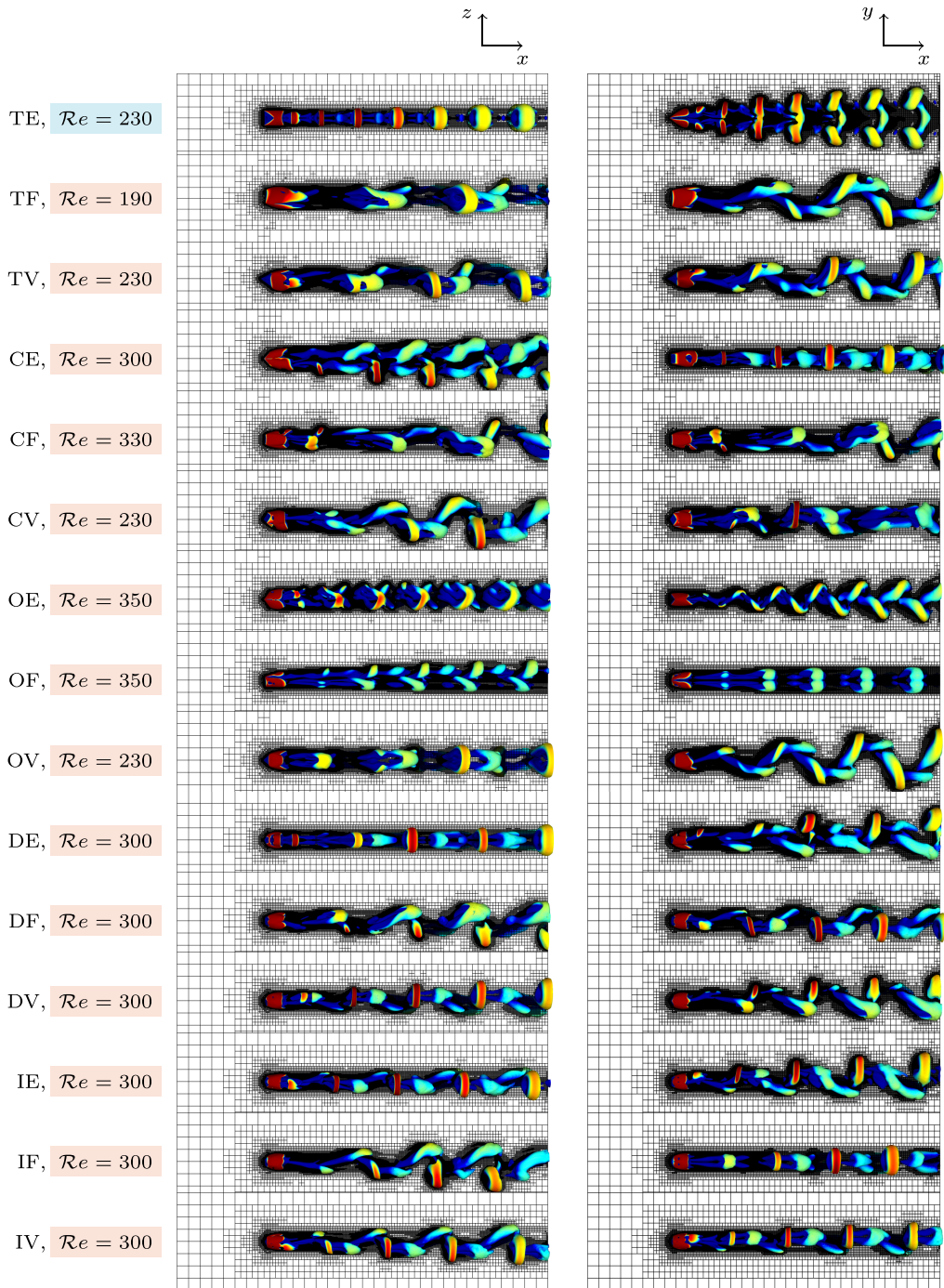


FIG. 12. Wake structures identified by the isosurface  $\lambda_2 = -1$  and colored by  $u_x$  in the flow in the HS/DHS regime in the  $x$ - $z$  plane (left) and in the  $x$ - $y$  plane (right).

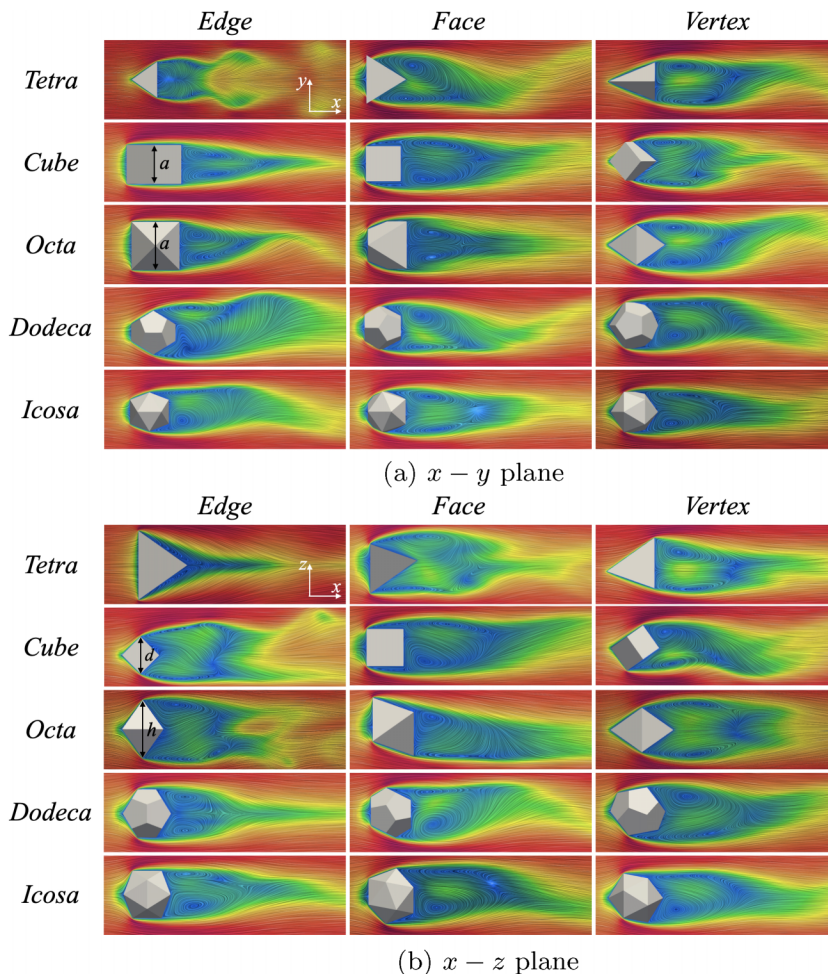


FIG. 13. LIC streamlines of the flow past a Platonic polyhedron at the three angular positions in the HS/DHS regime in the  $x$ - $y$  plane and in the  $x$ - $z$  plane. LIC streamlines are colored by the velocity magnitude (from min in blue to max in red).

The vortex shedding mode and frequency are closely related to the flow recirculation in the wake region. In Fig. 12, we notice several cases with high shedding frequency such as TE and OE (with six periods in the snapshot) and CE and OF (with five periods). According to our previous study [25], the crosswise cross-sectional surface area has similar values  $S_{pp,x} \approx 1 \sim 1.5$  for the Platonic polyhedrons at the three angular positions.  $S_{pp,x}$  affects the drag coefficient  $C_d$  in the steady regime, but plays a much less important role on the unsteady vortex shedding. We postulate that two geometric properties of the particle have a significant influence on the shape of the recirculation region: (i) the aspect ratio  $\chi$  of the crosswise cross-sectional surface area and (ii) the rear surface geometry of the particle. The particle with a larger aspect ratio  $\chi$  exhibits an oval recirculation region. Taking the example of the OE, we note that the width of the recirculation region in the  $x$ - $y$  plane in Fig. 13(a) is smaller than that in the  $x$ - $z$  plane in Fig. 13(b). This is due to the fact that the OE has a large aspect ratio  $\chi = h/a = \sqrt{2} \approx 1.4$ , where the height  $h$  denotes the distance between two opposite vertices and  $a$  is the edge length of the octahedron. The elongated geometry of OE exhibits a narrower recirculation region compared to that of other particles such as D and I in the  $x$ - $y$  plane. We observe a comparable scenario in the CE case. The aspect ratio  $\chi = d/a$

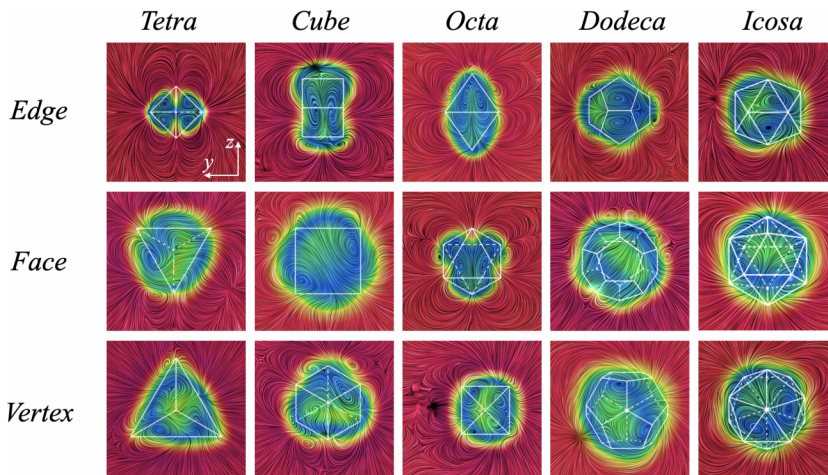


FIG. 14. LIC streamlines of the flow in the near-wake region of the Platonic polyhedron at the three angular positions in the HS/DHS regime in the  $y$ - $z$  plane located at  $x = x_p + 1$ . LIC streamlines are colored by the velocity magnitude (from min in dark blue to max in dark red) and particle edges are projected as white lines.

of the CE is also equal to  $\sqrt{2} \approx 1.4$ , leading to a narrower recirculation region in the  $x$ - $y$  plane in Fig. 13(a) than that in the  $x$ - $z$  plane in Fig. 13(b). The size of vortices is restricted by the limited volume of the recirculation region in the  $x$ - $y$  plane (CE, OE). Thus, the vortices need less time to reach a threshold size for the detachment from the wake region. Consequently, we observe a higher shedding frequency in Fig. 12.

A second factor that changes the shape of the recirculation region is the geometry of the particle rear surface. The crosswise cross-section of the isometric particle TE has an aspect ratio  $\chi = 1$  along the  $y$  and  $z$  axis. Also, the two rear faces of the TE guide the flow to converge smoothly in the particle wake which leads to a highly narrow recirculation region in the  $x$ - $z$  plane as shown in Fig. 13(b). A *U-shape* recirculation region manifests in the  $x$ - $y$  plane for the flow past a TE, where the middle section of the recirculation is much shorter than the two side arms. Consequently, the vortices formed in the limited-size side arms have a higher frequency of shedding in Fig. 12. The vortex pairs detach from the recirculation region easily and almost simultaneously due to the high level of symmetry of the TE, leading to double-hairpin vortex shedding (DHS). The high shedding frequency of the OF is deemed to be the collective effect of  $\chi = 1.15$  and the rear surface geometry. In contrast, the OV has the same aspect ratio  $\chi = 1$  and rear surface in both the  $x$ - $y$  and  $x$ - $z$  plane. The oval shape of the recirculation region in the OV case also has a slightly larger size than that in the OF case. Consequently, we observe a lower vortex shedding frequency than that in the OF case and the OV manifests a shedding mode similar to that observed for the sphere.

Figure 14 presents the snapshots of flow streamlines in LIC in the  $y$ - $z$  plane. Compared to Fig. 8, the wake streamlines shift from multiplanar symmetry to planar symmetry. In many cases, the streamlines fluctuate, and the planar symmetry is no longer maintained. The TE maintains a *quasiorthogonal* symmetry during vortex shedding, which then transitions to a planar symmetry with increasing  $Re$ . It is the only case where the high level of symmetry of vorticity is preserved in the unsteady regime (DHS-I). Several other particles maintain a planar symmetry in Fig. 14, such as the DE and the DV, the OF and the IV. Please note that the planar symmetry of the streamlines for these particles may be imperfect or even broken at other times. The fluctuations on the streamlines in the particle wake region contribute to the unsteadiness of the vortex shedding. In some cases, such as the IV at high Reynolds numbers  $Re = 340$  and  $370$ , the vortex shedding occurs in a stable plane. In other cases, the vortex shedding plane becomes time-dependent in time and space, such as

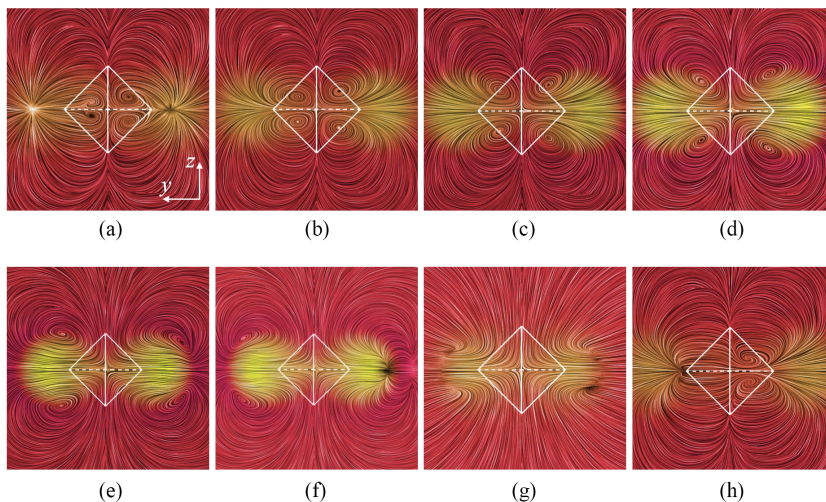


FIG. 15. LIC streamlines of the flow at  $Re = 200$  in the far field region of the TE in the  $y$ - $z$  plane at different distances from the particle: (a)  $x = x_p + 7.2$ , (b)  $x = x_p + 7.4$ , (c)  $x = x_p + 7.6$ , (d)  $x = x_p + 7.8$ , (e)  $x = x_p + 8.0$ , (f)  $x = x_p + 8.1$ , (g)  $x = x_p + 9.2$ , and (h)  $x = x_p + 11.6$ . LIC streamlines are colored by the flow velocity magnitude (from min in dark blue to max in dark red, same color map as in Fig. 14) and particle edges are projected as white lines.

in the TV case at  $Re = 200$  and the CV case at  $Re = 230$ . The asymmetry of the wake streamlines, as shown in Fig. 14, contributes to the rotation of the vortex shedding plane. The TV and the CV exhibit a time-dependent orientation of the vortex shedding plane even at the early stage of the HS regime. A plausible explanation is that they cannot maintain the planar symmetry of the streamlines in the wake region during the vortex shedding.

In addition to Fig. 13, we present the recirculation region behind the Platonic polyhedrons in the  $y$ - $z$  plane in Fig. 14. In the TE, CE, OE and OF cases, which exhibit a relatively high frequency of vortex shedding, the recirculation region has a markedly ovoid shape dictated by the crosswise surface area. Moreover, in the TE and OF cases, the recirculation area is smaller than the projected particle outline. The particles with low vortex shedding frequency present a recirculation region with mostly a spherical or triangular shape in the  $y$ - $z$  plane. This confirms our postulate that the vortex shedding frequency is determined by the shape and size of the recirculation region, which reflects the particle angularity and angular position.

### 3. Vortex spatial evolution

To gain deeper insight, we compare the spatial evolution of two types of vortex shedding: double-hairpin vortex shedding (DHS) in the TE case and the single-hairpin vortex shedding (HS) in the DV case.

Figure 15 gives the far-wake streamlines in LIC of the flow at  $Re = 200$  past the TE in the  $y$ - $z$  plane, which features a double-hairpin vortex shedding (DHS). We take snapshots of an entire period of the shedding progress in space along the streamwise  $x$  direction. First, two pairs of opposite-signed vortices are generated from the center of the particle wake in Fig. 15(a). The hairpin vortex pair on the left is slightly smaller than the one on the right, but both maintain symmetry with respect to the  $x$ - $y$  plane. A little bit farther, we notice the appearance of two circular low-velocity regions (in light yellow), symmetric with respect to the  $x$ - $z$  plane. These two low-velocity regions become more evident with increasing distance  $x$  from the particle and the two pairs of vortices begin to move away from the centerline, with their centers shifting around the rim of the two low-velocity regions. Simultaneously, the vortices increase in size as they move toward the far end (with respect

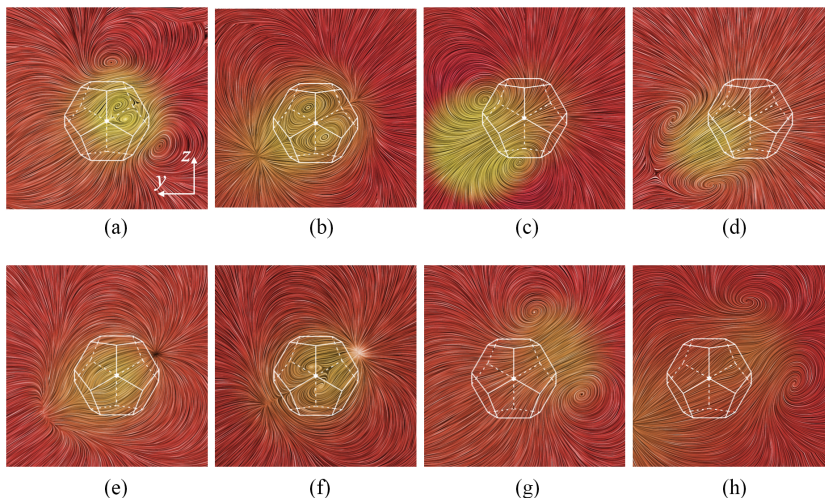


FIG. 16. LIC streamlines of the flow at  $Re = 300$  in the far field region of the DV in the  $y$ - $z$  plane at different distances from the particle: (a)  $x = x_p + 5.5$ , (b)  $x = x_p + 5.6$ , (c)  $x = x_p + 6.2$ , (d)  $x = x_p + 7.8$ , (e)  $x = x_p + 8.8$ , (f)  $x = x_p + 9.2$ , (g)  $x = x_p + 11.2$ , and (h)  $x = x_p + 12$ . LIC streamlines are colored by the flow velocity magnitude (from min in dark blue to max in dark red, same color map as in Fig. 14) and particle edges are projected as white lines.

to the centerline) of the low-velocity regions. As shown in Fig. 15(e), the larger vortex pair touches the far end of the low-velocity region and then vanishes in Fig. 15(f). The same process is repeated by the smaller vortex pair on the left in Fig. 15(f). As we move further away from the particle, we observe an older pair of vortices created by the previous shedding process. Figure 15 highlights two important phenomena: (i) the two hairpin vortices in the DHS regime have a slight difference in size in the far-wake region of the particle. This difference, although subtle, is more clearly visible in LIC streamlines behind the particle, as compared to the visualization using  $\lambda_2$  or  $\omega_x$  isosurfaces; (ii) the velocity field downstream the TE maintains a high level of planar symmetry, which contributes to the stability of the double-hairpin vortex structure during the shedding process.

As an illustration of the single-hairpin vortex shedding in the HS regime, the far-wake LIC streamlines of the flow at  $Re = 300$  past the DV in the  $y$ - $z$  plane are depicted in Fig. 16. During the vortex shedding process, the far-wake velocity field maintains a high level of planar symmetry. First, a pair of small vortices are generated in the center region, accompanied by a pair of larger vortices coming from the previous period of shedding in Fig. 16(a). A direct comparison with Fig. 15 reveals that there exists only one circular low-velocity region (in light yellow) that oscillates around the centerline. The small vortices grow in size while moving away from the centerline, along the rim of the low-velocity region in Figs. 16(b)–16(d). Then, the vortex pair disappears at the far end of the low-velocity region, marking the end of the first half-period in Fig. 16(e). Subsequently, a second pair of vortices appear in the center region. It follows a similar dynamic process as the first vortex pair, but moves in the opposite direction as shown in Figs. 16(f)–16(h). The two circular low-velocity regions in Fig. 15 can be attributed to the two side arms of the *U-shape* recirculation region in the TE case. In contrast, we see an oval recirculation region in the wake of the DV in Fig. 14, leading to a single low-velocity region in Fig. 16. This once again highlights the impact of the shape and size of the recirculation region on the vortex shedding mode.

### E. Recirculation and vortex shedding frequency

We plot the Strouhal number  $St$  as a function of  $Re$  in the HS regime and the early stage of the CS regime in Fig. 17(a) and show the influence of particle angularity on the vortex shedding frequency.  $St$  is computed using the temporal evolution of the lift coefficient along either the  $y$  axis

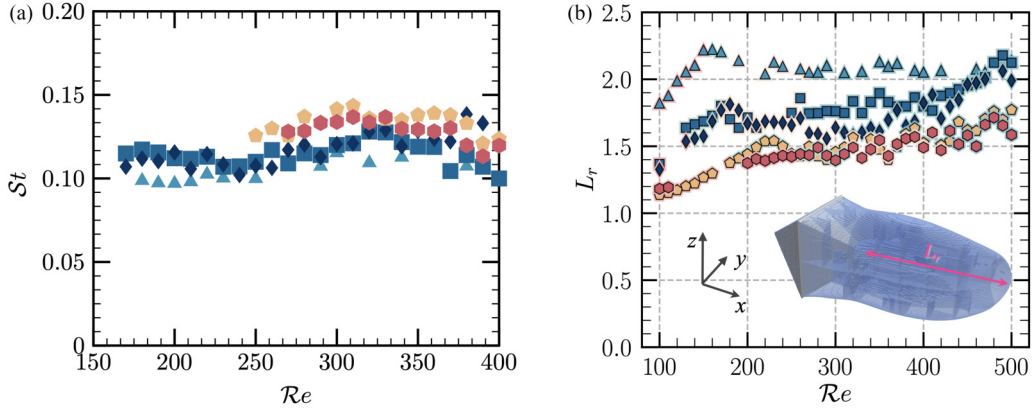


FIG. 17. (a)  $St$  of Platonic polyhedrons at the vertex angular position as a function of  $Re$ ; (b)  $L_r$  as a function of  $Re$  in the wake of a Platonic polyhedron at the vertex angular position: TV ( $\blacktriangle$ ), CV ( $\blacksquare$ ), OV ( $\blacklozenge$ ), DV ( $\blacklozenge$ ), and IV ( $\blacklozenge$ ); markers highlighted with flow regimes: MSS ( $\color{red}\blacksquare$ ), PSS ( $\color{green}\blacksquare$ ), HS ( $\color{orange}\blacksquare$ ), and CS ( $\color{blue}\blacksquare$ ).

or the  $z$  axis ( $C_{l,y}$  or  $C_{l,z}$ , respectively) according to the vortex shedding plane. In the HS regime, we compute the dominant frequency of the shedding using fast Fourier transform (FFT) by carefully choosing a number of periods of oscillation once the vortex shedding regime is well established, to get an accurate estimation of  $St$ . Please note that the dominant frequency in the CS regime varies at different time intervals as the vortex shedding in the CS regime is highly disordered. We count the number of hairpin vortices detached from the particle rear surface over a time interval to compute  $St$ , which leads to slightly different values than simply identifying the dominant frequency in the FFT frequency spectrum. The values reported for  $St$  in the CS regime are, therefore, approximate and presented to show a general trend. In general, for all the Platonic polyhedrons at the vertex angular position, the variation of  $St$  is not significant and remains between 0.1 and 0.15 for  $150 \leq Re \leq 400$ . It was reported that  $St = 0.135$  for a flow past a fixed sphere [17], which is consistent with our findings. In the range of Reynolds numbers  $200 \leq Re \leq 250$ , the particles with high angularity (TV, CV, OV) exhibit single-hairpin vortex shedding with an almost constant  $St \approx 0.1 \sim 0.12$ .  $St$  has slightly higher values in the CV case and lower values in the TV case. With the onset of the CS regime ( $Re = 270$  in the TV and CV cases and  $Re = 310$  in the OV case),  $St$  shows a very mild increase tendency. At  $250 \leq Re \leq 350$ , the HS regime starts for the particles with high sphericity (DV and IV), where the  $St$  has slightly higher values than that in the TV, CV, and OV cases.

We calculate and plot the length of the recirculation region ( $u_x \leq 0$ ), denoted  $L_r$ , as a function of  $Re$  for the five Platonic polyhedrons at the vertex angular position in Fig. 17(b). For measurement consistency, we define  $L_r$  as the distance from the rear vertex of the particle to the farthest cell possessing zero or negative streamwise velocity as illustrated in the CV case in Fig. 17(b). To emphasize the relationship between  $L_r$  and regime transitions, we outline the markers with colors corresponding to the respective regimes in Table I. The TV displays the longest  $L_r$  across the range  $100 \leq Re \leq 500$ . As the sphericity  $\phi$  increases,  $L_r$  correspondingly decreases. The pairs CV/OV and DV/IV share similar sphericity values and exhibit comparable  $L_r$ . At  $Re \leq 200$ ,  $L_r$  increases with  $Re$  for all particles within the MSS and PSS regimes. However, in the HS regime, a reduction in  $L_r$  is observable in the TV, CV, and OV cases. In the CS regime,  $L_r$  tends to increase with  $Re$  for all Platonic polyhedrons.

In the five vertex cases, the flow recirculation region has an oval cross-sectional shape of similar size as shown in Figs. 8 and 14, thus leading to similar  $St$  in Fig. 17(a). However, the angular position of the particle can greatly influence the shape of the recirculation region and, subsequently, the vortex shedding frequency. This is particularly evident in the TE and OE cases, where the hairpin vortex shedding is characterized by  $St \approx 0.2$ . To demonstrate quantitatively the significant influence

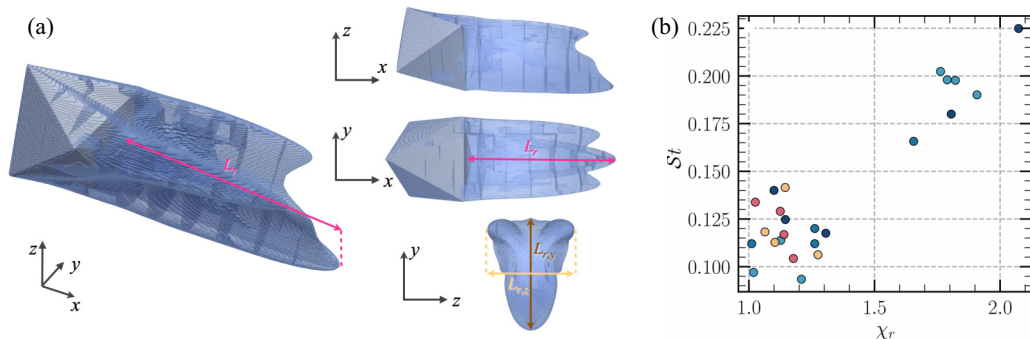


FIG. 18. Recirculation region and vortex shedding frequency: (a) size of the recirculation region in the OF case at  $Re = 350$ ; (b)  $St$  as a function of the aspect ratio  $\chi_r$  of the recirculation region at  $x = x_p + 1$ : T (●), C (●), O (●), D (●), and I (●).

of the recirculation region [blue region in Fig. 18(a)], we compute and analyze its aspect ratio defined as

$$\chi_r = \frac{\max(L_{r,y}, L_{r,z})}{\min(L_{r,y}, L_{r,z})}, \quad (20)$$

where  $L_{y,r}$  and  $L_{z,r}$  represent the size of the recirculation region along the  $y$  and  $z$  axes at  $x = x_p + 1$  as depicted in Fig. 18(a). With this definition,  $\chi_r$  always remains equal to or larger than 1. We select 24 representative cases of particles at various angular positions in the DHS/HS regime, among those presented in Figs. 12–14. We observe that the volume of recirculation in the DHS/HS regime inversely correlates with the particle sphericity  $\phi$  at the same  $Re$ , which agrees with Fig. 17(b). In Fig. 18(b), we illustrate how the dominant vortex shedding frequency  $St$  is influenced by  $\chi_r$  at  $x = x_p + 1$ . For instance, when  $\chi_r$  is close to 1,  $St$  ranges from 0.1 to 0.15, matching the results in Fig. 17(a). As  $St$  is also dependent on other parameters such as particle shape and  $Re$ , a considerable number of data points are located in the bottom left of Fig. 18(b). In contrast, for  $\chi_r \geq 1.5$ , we notice a marked increase in  $St$ , rising to 0.2 or higher in the TE, CE, and OE cases. As discussed in Fig. 14, a larger particle aspect ratio  $\chi$  yields higher values of  $\chi_r$ , which diminishes the *effective* volume of the recirculation region. This results in a discernible reduction in both vortex size and vortex residence time in the particle wake, leading to an increased vortex shedding frequency in the cases on the right top of Fig. 18(b).

### F. Drag and lift coefficients

For the sake of conciseness, we primarily focus on the vertex angular position (V) from now on and examine the impact of particle angularity. We report in Fig. 19 the time-averaged drag coefficient  $\overline{C_d}$  as a function of  $Re$  in the interval  $100 \leq Re \leq 500$  for all five Platonic polyhedrons as well as the sphere. In the unsteady flow regimes (HS and CS), the drag force becomes time-dependent due to the vortex shedding and  $\overline{C_d}$  is time averaged once the flow regime is well established. In general,  $\overline{C_d}$  decreases monotonously with  $Re$  for all Platonic polyhedrons and the sphere. There is a distinct gap between the  $\overline{C_d}(Re)$  curves of two types of particles. The  $\overline{C_d}(Re)$  curves of the particles of high angularity (TV, CV, and OV) always lie well above the  $\overline{C_d}(Re)$  curves of the particles with high sphericity (DV and IV), for any  $Re \in [100, 500]$ . At  $100 \leq Re \leq 200$ ,  $\overline{C_d}$  decreases with the particle sphericity  $\phi$ , i.e., the more spherical a particle is, the lower its  $\overline{C_d}$  is ( $\overline{C_d,TV} > \overline{C_d,CV} > \overline{C_d,OV} > \overline{C_d,DV} > \overline{C_d,IV}$ ). Then the TV tends to have a smaller  $\overline{C_d}$  compared to that of the CV and the OV when  $Re > 250$ . The particle angularity is no longer a determinant factor of the magnitude of  $\overline{C_d}$  in this case. Instead, the particle angular position has a more pronounced impact on  $\overline{C_d}$  at high  $Re$ , which was also reported in our previous work on the tetrahedron

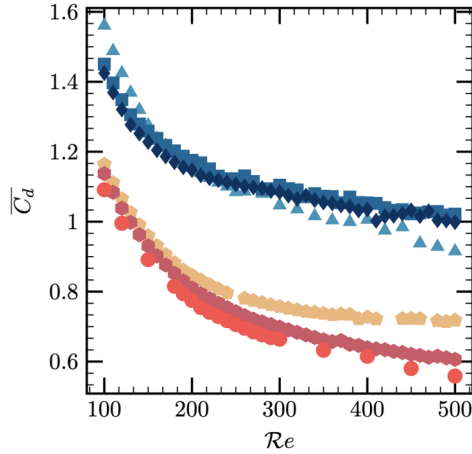


FIG. 19.  $\overline{C_d}$  of Platonic polyhedrons at the vertex angular position as a function of Re: TV ( $\blacktriangle$ ), CV ( $\blacksquare$ ), OV ( $\blacklozenge$ ), DV ( $\bullet$ ), and IV ( $\bullet$ ), and the sphere ( $\bullet$ ).

[43]. For particles of high sphericity (DV, IV),  $\overline{C_d}$  approaches the value of the flow past a fixed sphere. Especially the IV has a very close  $\overline{C_d}$  to that of a sphere, with a maximum difference of approximately 8%.

The time evolution ( $t = t^*/t_{\text{ref}}^*$ ) of  $C_{l,y}$  and  $C_{l,z}$  in the CV and OV cases, as two representatives of a particle with high angularity, is plotted in Fig. 20 at Re from the end of the MSS regime to the early stage of the HS regime. In the MSS regime, both  $C_{l,y}$  and  $C_{l,z}$  have values close to zero. As Re increases, the PSS regime begins and we observe an increase of  $C_{l,y}$  at Re = 150 and of  $C_{l,z}$  at Re = 140 in Fig. 20(a). In the PSS regime,  $C_{l,y}$  and  $C_{l,z}$  increase temporarily before reaching a stable time average value.  $C_l$  has a preferred direction in the CV case with  $C_{l,y} > 0$  and  $C_{l,z} > 0$ . In contrast, the OV shows a distinct change in lift direction with increasing Re as depicted in Fig. 20(b). At Re = 140,  $C_l$  maintains a stable value in the  $y^-$  direction ( $C_{l,y} < 0$  and  $C_{l,z} \approx 0$ ), but at Re = 150 it shifts to the  $z^+$  direction ( $C_{l,y} \approx 0$  and  $C_{l,z} > 0$ ). This switch of lift direction can be attributed to the alteration of the symmetry plane in the PSS regime. During the transition from the MSS regime to the PSS regime, the wake structure selects one of the symmetry planes in the MSS regime. From Re = 170 to Re = 180, instead of a smooth curve, we see the  $C_{l,y}$  and  $C_{l,z}$  oscillate with a single frequency in the CV case in Fig. 20(a), marking the onset of the HS regime. We observe the same transition from the PSS regime to the HS regime on the lift curves in Fig. 20(b), where  $C_{l,y}$  increases and then oscillates around a stable value in the  $y^+$  direction while  $C_{l,z}$  increases temporarily before settling back to a near-zero value while oscillating.

In general, at a higher Re, the transient evolution of  $C_{l,y}$  and  $C_{l,z}$  becomes faster. However, the establishment of the flow regime requires a particularly long time when Re is close to the critical Reynolds number  $\text{Re}_{\text{cr}}$ . In Fig. 20, we see that the PSS regime requires  $t = 200$  to reach a steady state at Re = 150, whereas it takes approximately  $t = 1000$  in the OV case to establish the PSS regime at Re = 160 and the HS regime at Re = 170. In addition, in the TV, CV and OV cases, the transition time is relatively short compared to the particle with high sphericity.

Figure 21 illustrates the time evolution of  $C_{l,y}$  and  $C_{l,z}$  in the DV and IV cases.  $C_{l,y}$  and  $C_{l,z}$  maintain the same direction throughout the range of Re from the MSS regime to the HS regime. In the range of Re presented, we see that  $C_{l,y}$  remains negative in both the DV case and the IV case.  $C_{l,z}$  has positive values in the DV case but negative values in the IV case. The switch of lift direction during the transition from the MSS regime to the HS regime in the OV case is not observed in the DV and IV cases. Similar to the particles of high angularity (T, C, O),  $C_{l,y}$  and  $C_{l,z}$  have near-zero values in the MSS regime at low Re such as Re = 180 in the DV case and Re = 200 in the IV case. In the

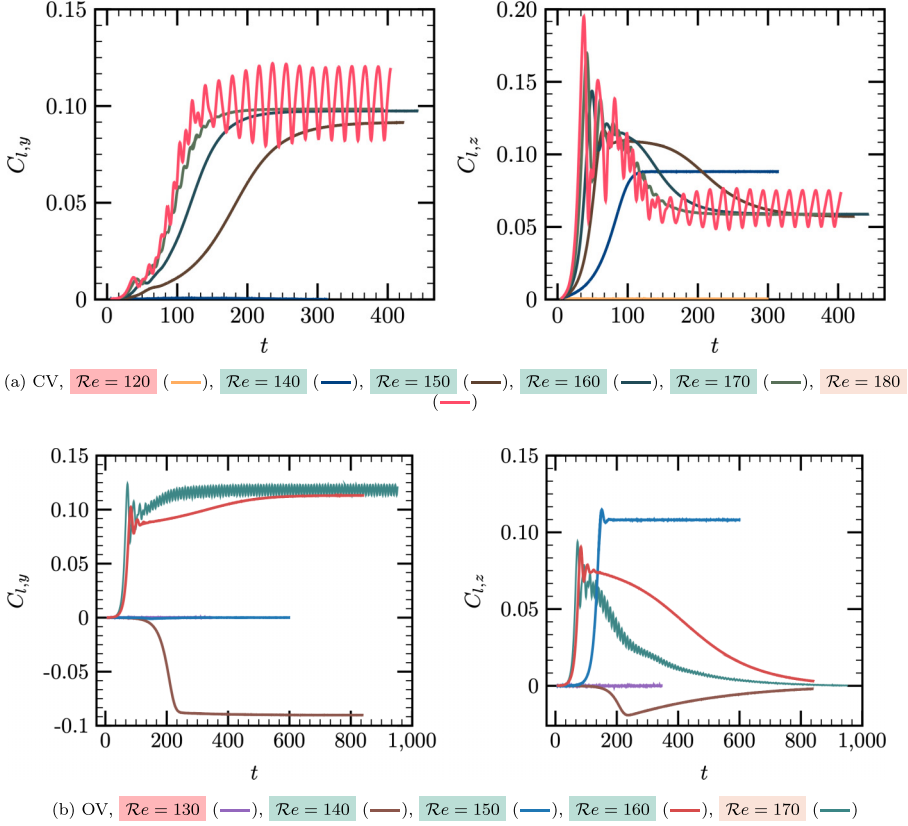


FIG. 20. Time evolution of  $C_{l,y}$  and  $C_{l,z}$  of the CV and of the OV during the transition from the MSS regime to the HS regime.

PSS regime in the DV case,  $C_{l,y}$  increases continuously to a stable value, while  $C_{l,z}$  initially increases and then returns to a lower stable value in the range  $190 \leq Re \leq 240$ . As a key characteristic of the PSS regime, the significant increase of  $C_l$  is observed with increasing  $Re$ . In contrast to Fig. 20, it is not necessarily the case that the transition to the steady state is faster at higher  $Re$  in the DV and IV cases. From  $Re = 210$  to  $Re = 240$  in Figs. 21(a), we see that the transient time increases with  $Re$  for both  $C_{l,y}$  and  $C_{l,z}$  in the DV case. In the IV case,  $C_{l,y}$  at  $Re = 220$  reaches its steady-state value at about  $t = 300$ , whereas we need to wait until  $t = 1700$  for  $C_{l,y}$  to reach its steady state value at  $Re = 240$ . The regime establishment requires a long time when the  $Re$  becomes close to the critical value of the transition from the PSS regime to the HS regime. We need about  $t = 1500$  for  $C_{l,y}$  to reach the steady state at  $Re = 250$  in the IV case, which is longer than the CV and OV cases. In the DV case, the time required for the establishment of the HS regime is even longer than  $t = 1800$  at  $Re = 250$  in Fig. 21(a).  $C_{l,y}$  and  $C_{l,z}$  start oscillating around their stable value in the HS regime, depicted by, e.g.,  $Re = 250$  in the DV case and  $Re = 270$  in the IV case.

To clearly depict the time evolution of the lift force, we plot the phase diagram of  $C_{l,y}$  versus  $C_{l,z}$  from the MSS regime to the HS regime. We select two particles of high angularity (CV, OV) and two particles of high sphericity (DV, IV) in Fig. 22, given that the tetrahedron cases are analyzed in detail in the companion paper of the present work [43]. The rainbow color of the curves (from purple to red) indicates a time increase. In the MSS regime, the transverse force is small due to the flow symmetry and the two components  $C_{l,y}$  and  $C_{l,z}$  are randomly distributed in space. As soon as the PSS regime starts,  $C_l$  has a preferred direction as shown in Fig. 22(a), where  $C_{l,y}$  and

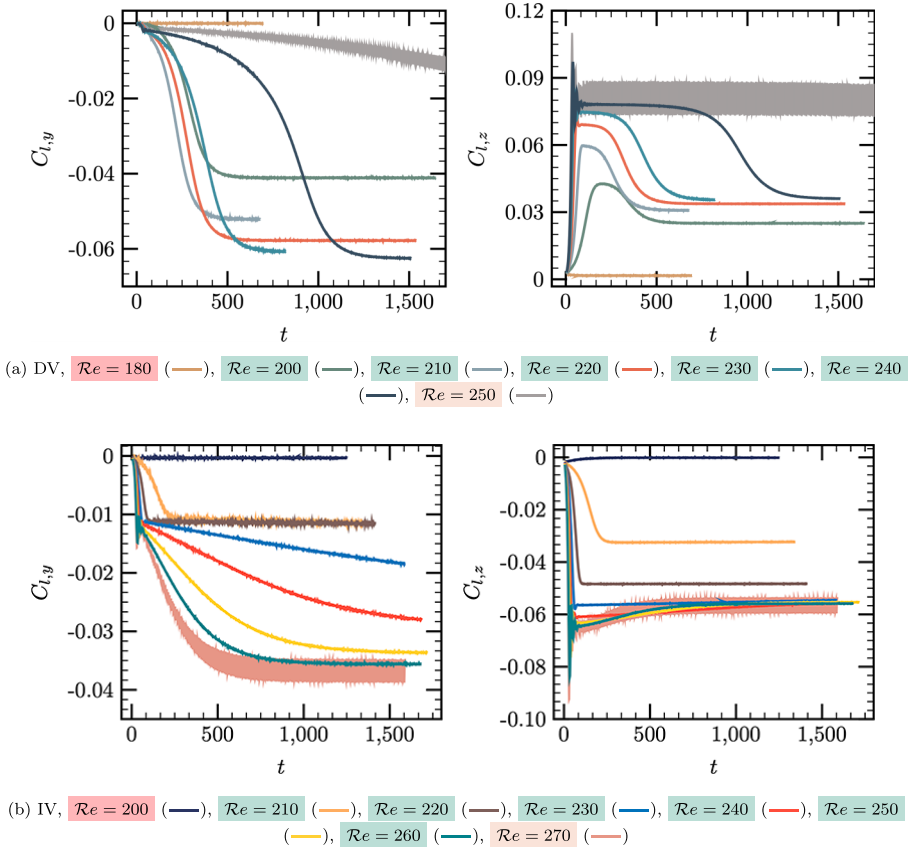


FIG. 21. Time evolution of  $C_{l,y}$  and  $C_{l,z}$  of the DV and of the IV during the transition from the MSS regime to the HS regime.

$C_{l,z}$  increase and reach a stable value depicted by the red dots. This process is followed by all the Platonic polyhedrons in the PSS regime, as shown in Figs. 22(e), 22(i), and 22(m). With increasing  $\mathcal{Re}$ , the  $C_{l,y}$ - $C_{l,z}$  curve becomes wavy and fluctuates in Figs. 22(b) and 22(c). However, we still observe a stable value of  $C_l$  given a long enough simulation time. Subsequently, in the CV case at  $\mathcal{Re} = 180$ ,  $C_l$  oscillates around a fixed value represented by the red curve as shown in Fig. 22(d). The CV is now ready for the onset of the HS regime. At  $\mathcal{Re} = 180$ , it is difficult if not impossible to observe clear hairpin vortex structures using  $\lambda_2$  or  $\omega_x$  isosurfaces, even though the lift force has begun oscillating, but they are clearly observed at  $\mathcal{Re} = 190$ .

In the OV case, we see a clear transition from the PSS regime to the HS regime in Figs. 22(f)–22(h). In the PSS regime, the lift coefficients converge to a fixed value smoothly at  $\mathcal{Re} = 160$ . At a higher  $\mathcal{Re}$ , the lift coefficients undergo a similar transition process as in the CV case and then start to oscillate at  $\mathcal{Re} = 170$ , marking the onset of the HS regime. We observe a clear hairpin vortex shedding at  $\mathcal{Re} = 170$  using the  $\lambda_2 = -1$  isosurface. The vortex shedding is also depicted in Figs. 22(g) and 22(h), where we see the *spring-shaped* trajectory of  $C_l$  in red.  $C_{l,z}$  drops to a very small value while  $C_{l,y}$  oscillates around a fixed value at  $\mathcal{Re} = 170$  and  $\mathcal{Re} = 180$ . Eventually, the shedding of hairpin vortices occurs in the  $x$ - $y$  plane, with a higher oscillation amplitude at  $\mathcal{Re} = 180$ .

In the case of particles with high sphericity (DV, IV), the transition process is similar.  $C_{l,y}$  and  $C_{l,z}$  start oscillating at  $\mathcal{Re} = 250$  and  $\mathcal{Re} = 270$  in the DV case and the IV case, respectively, as shown in Figs. 22(j) and 22(n). Then the amplitude of the oscillation increases with  $\mathcal{Re}$ . In the DV

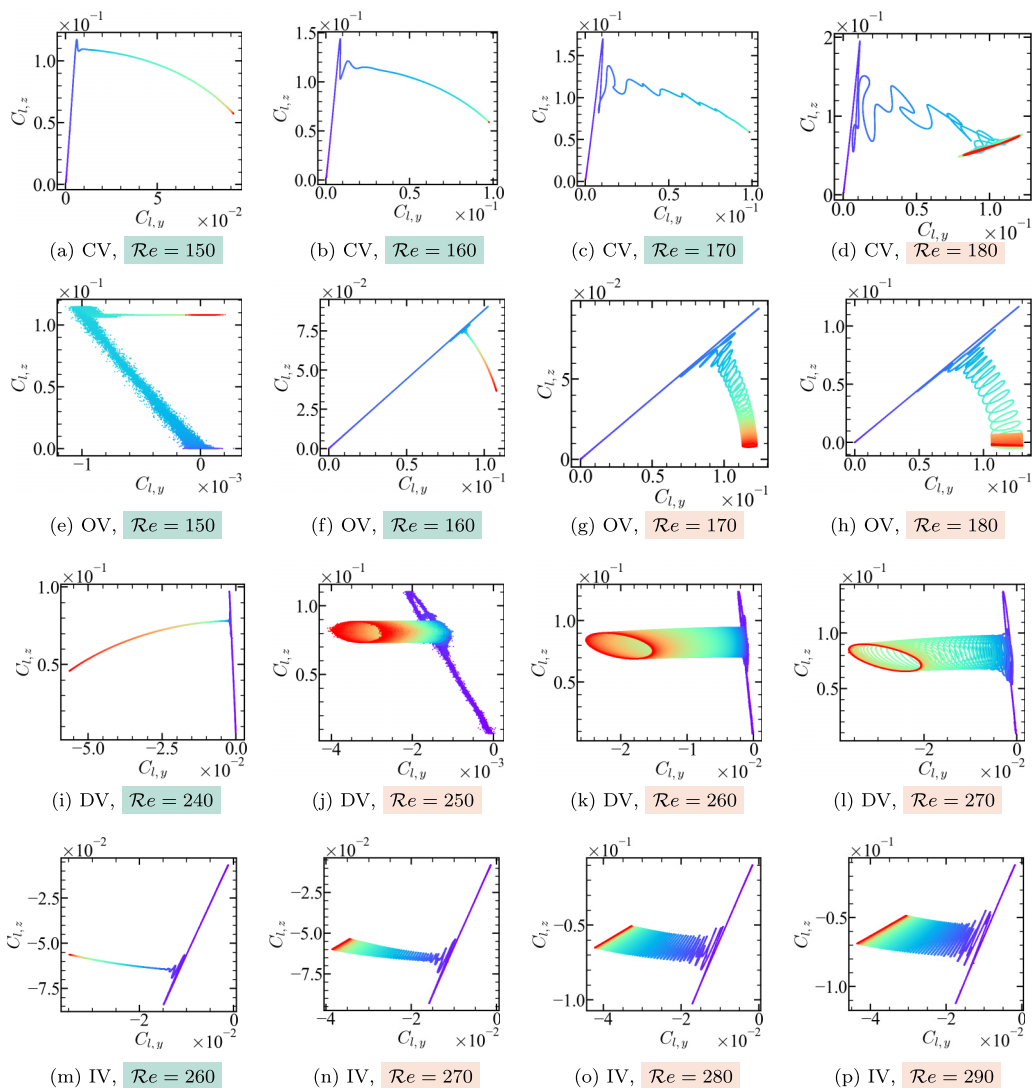


FIG. 22.  $C_{l,y}$ - $C_{l,z}$  phase diagram of Platonic polyhedrons at the vertex angular position, comparison between the PSS regime and the HS regime. Time evolution given in rainbow color from purple (start time) to red (end time).

case, we see a red elliptical trajectory in Figs. 22(j)–22(l), which indicates that the direction of the hairpin vortex shedding rotates in the  $y$ - $z$  plane. The shedding plane keeps oscillating between two stable planes of symmetry. In contrast, we only see a red straight line for the trajectory of the lift coefficient in the IV case in Figs. 22(n)–22(p). This is a special case of hairpin vortex shedding, where the shedding plane is very stable and almost *fixed* in the  $C_{l,y}$ - $C_{l,z}$  phase diagram. According to previous studies, the hairpin vortex shedding in the flow past a sphere exhibits a *fixed-orientation* shedding plane [17], which is also observed here in the IV case. Consequently, the icosahedron (I) has many similarities with the sphere, such as  $\overline{C_d}$ , wake symmetry and shedding modes, due to its high sphericity  $\phi = 0.94$ .

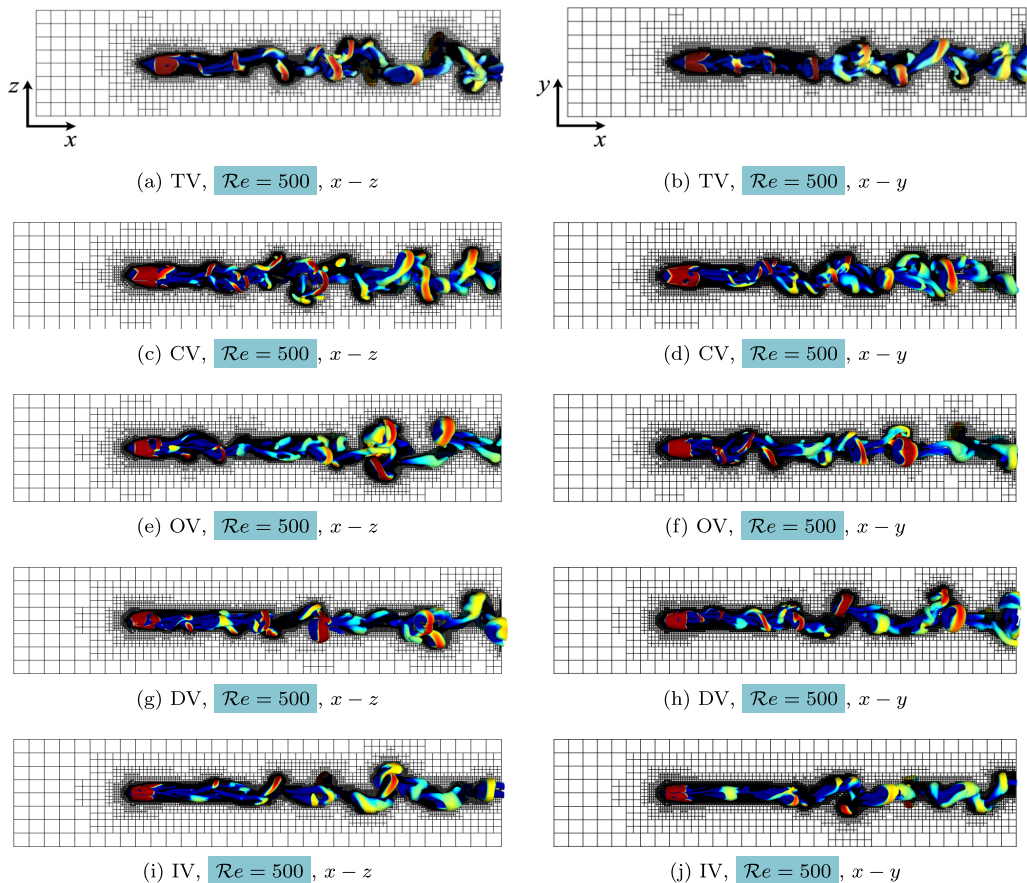


FIG. 23. Wake structures identified by the isosurface  $\lambda_2 = -1$  and colored by  $u_x$  in the flow past a Platonic polyhedron in the CS regime in the  $x$ - $z$  plane (left) and in the  $x$ - $y$  plane (right).

### G. Chaotic vortex shedding

At high  $Re$ , the periodic vortex shedding starts to become disorganized with the onset of the CS regime. In the CS regime, the vortex structures are more dynamic and irregular than in the HS regime. The lift force also becomes less predictable and may fluctuate chaotically, and the frequency spectra of the vortex shedding may contain multiple secondary frequencies and vary over time in the CS regime.

#### 1. Chaotic vortex shedding modes

We show the vortex structures in the CS regime in Fig. 23. For consistency with Figs. 2 and 12, the vortex structures are again identified as isosurfaces of  $\lambda_2 = -1$  in the  $x$ - $z$  plane and the  $x$ - $y$  plane. In general, akin to the HS regime, the hairpin vortices in the CS regime are shed alternatively but disorganedly. Compared to Fig. 12, we see that these hairpin vortices are more intricately intertwined and contain small coherent structures in the flow past a particle of high angularity, such as TV, CV, and OV as shown in Figs. 23(b), 23(c), 23(d), and 23(e). These small vortex structures are generated from the breaking of the larger hairpin vortices or by the instabilities in the particle wake flow, when the flow recirculation region becomes chaotic and has irregular and unpredictable fluctuations. They have significant effects on the overall flow behavior characterized by the vortex shedding frequency and the hydrodynamic forces exerted on the particle. At  $Re = 500$ , the small

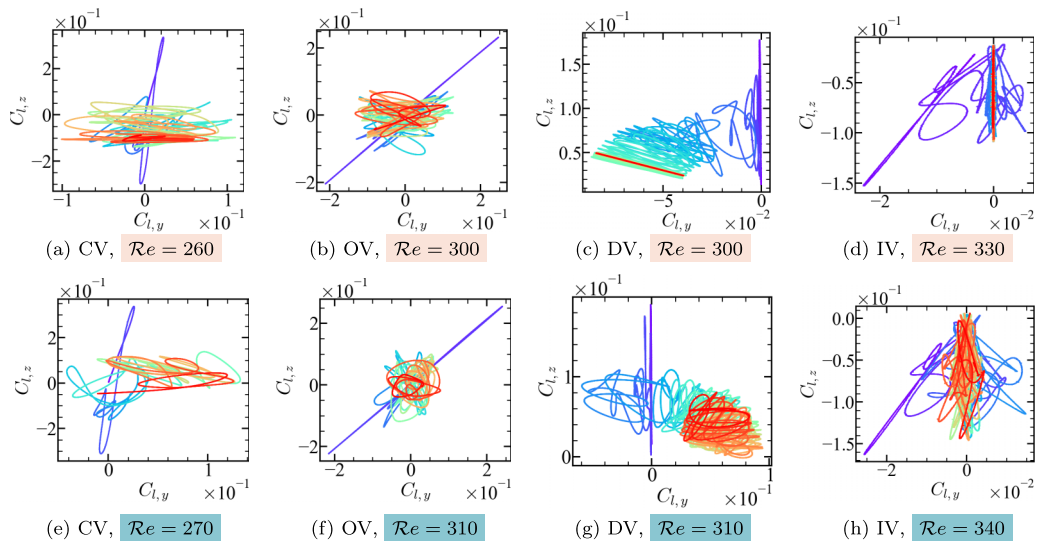


FIG. 24.  $C_{l,y}$ - $C_{l,z}$  phase diagram of Platonic polyhedrons at the vertex angular position, comparison between the HS regime and the CS regime. Time evolution given in rainbow color from purple (start time) to red (end time).

vortex structures are less evident for particles with high sphericity such as the IV. In Figs. 23(i) and 23(j), we still observe the bulky hairpin vortices, even though they shed randomly from the particle wake region. We know from Table I that the flow past the IV transitions to the CS regime at  $Re = 340$ . The CS regime in the IV case at  $Re = 500$  is less developed than in the CV case in which the CS regime begins at  $Re = 270$ . At a higher  $Re$ , the recirculation region becomes further unstable and the quantity of small coherent structures increases. The energy that was previously used to form large vortex structures is instead used to form smaller, less organized and more numerous structures. From a computing viewpoint, the advantage of the adaptive grid refinement is clearly demonstrated in Fig. 23. The regions with significant changes in velocity gradient are properly refined to have a more accurate description of the chaotic vortices at a relatively low computational cost.

## 2. Phase diagrams and shedding frequency

We compare the  $C_{l,y}$ - $C_{l,z}$  phase diagrams in the HS regime to those in the CS regime in Fig. 24. We observe in Fig. 24(a) that the vortex shedding in the CV case in the HS regime at  $Re = 260$  occurs in the  $x$ - $y$  plane. The preferred direction along the  $y$  axis disappears in the CS regime at  $Re = 270$ , as depicted in Fig. 24(e), where the  $C_l$  changes its direction randomly over time in the  $y$ - $z$  plane. In the HS regime, the hairpin vortex shedding shifts its plane but still has a preferred direction over a long time interval in the OV case. More specifically, even though the shedding plane keeps oscillating around the  $x$  axis, the vortex shedding happens mostly in the  $x$ - $y$  plane in Fig. 24(b). As  $Re$  increases,  $C_l$  loses its preferred direction in the CS regime as shown in Fig. 24(f). In both the HS regime and the CS regime,  $C_l$  in the OV case has a smaller amplitude than that in the other particles. For particles with high sphericity, Figs. 24(c) and 24(g) show the  $C_l$  time evolution in the DV case at  $Re = 300$  and  $Re = 310$ , respectively.  $C_l$  keeps its preferred direction along the  $y$  axis at  $Re = 300$ . However, at  $Re = 310$ ,  $C_l$  turns to be randomly oriented in the  $y$ - $z$  plane. We notice a clear transition from the HS regime to the CS regime from the  $C_{l,y}$ - $C_{l,z}$  phase diagram. In the IV case, we see a fixed plane of periodic vortex shedding at  $Re = 330$  once the HS regime is established as shown in Fig. 24(d), whereas at  $Re = 340$ , the vortex shedding plane changes over time and the orientation of  $C_l$  becomes erratic, indicating the onset of the CS regime.

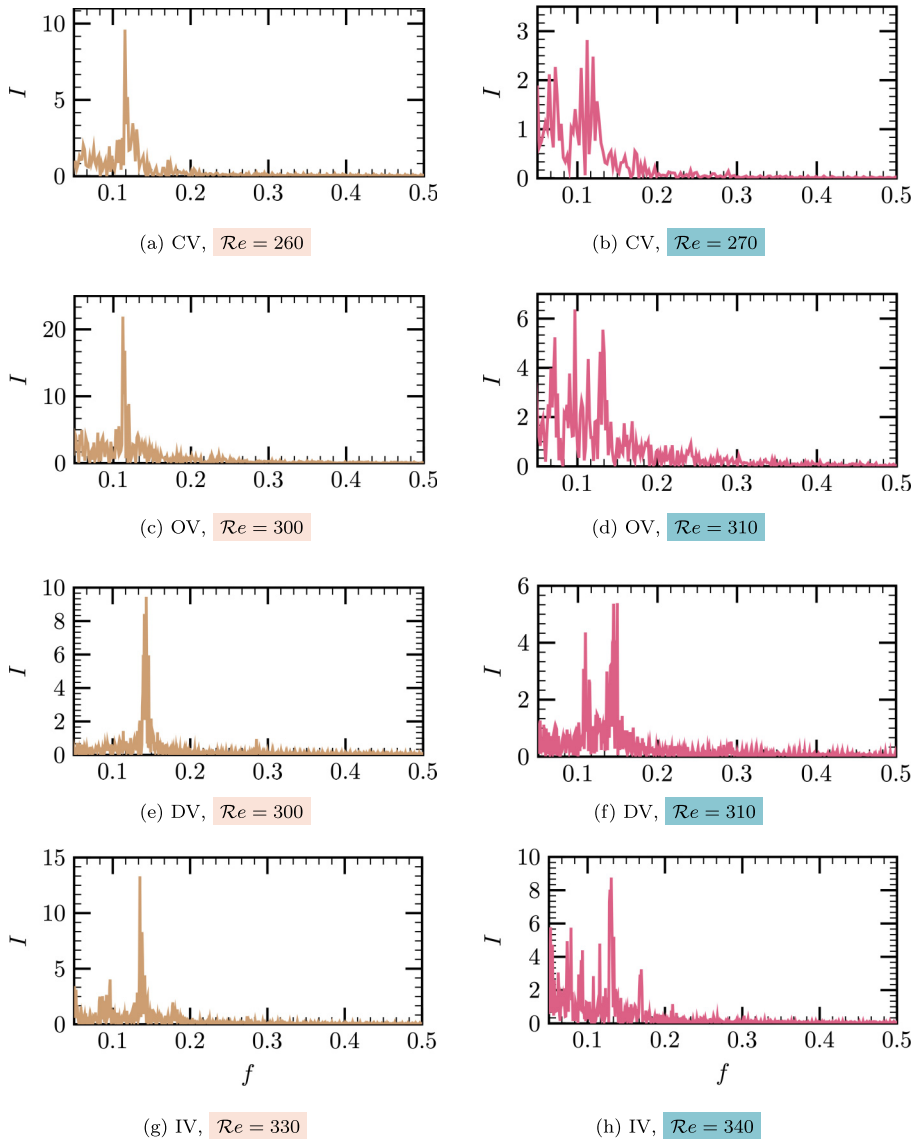


FIG. 25. Vortex shedding frequency  $f$  spectrum in the HS regime (■) and in the CS regime (■).  $I$  denotes the dimensionless frequency intensity obtained by FFT.

Figure 25 illustrates the vortex shedding frequency spectrum  $f = f^* D_{\text{sph}}^* / U_0^*$  of flow in the HS and CS regimes. These frequency spectra are obtained using classical FFT. The  $Re$  chosen in Fig. 25 are the same as in Fig. 24 for a better comparison. We observe that in the HS regime, the dominant oscillation frequency of  $C_{l,y}$  and  $C_{l,z}$ , that represents the vortex shedding frequency in the particle wake region, has a single peak with  $f \approx 0.12$ – $0.14$ , in line with the  $St$  plot of Fig. 17(a). As  $Re$  increases, the intensity of the secondary frequencies amplifies, marking the onset of the CS regime. Identifying the CS regime is challenging, as it requires multiple indicators such as: the deformation of vortex structure identified by  $\lambda_2$  or  $\omega_x$  isosurfaces, the variation of lift coefficient components and the appearance of multiple high-intensity frequencies. For example, the vortex structures identified by the  $\lambda_2$  isosurfaces reveal the disorganization, degeneration of the hairpin vortices, and the

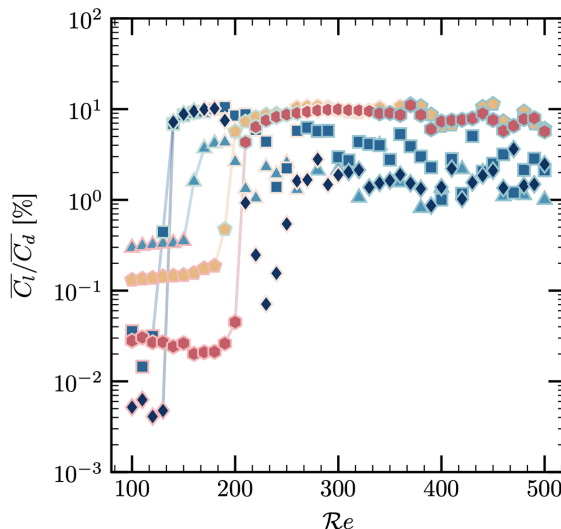


FIG. 26.  $\overline{C_l}/\overline{C_d}$  of Platonic polyhedrons at the vertex angular position as a function of  $Re$ : TV ( $\blacktriangle$ ), CV ( $\blacksquare$ ), OV ( $\blacklozenge$ ), DV ( $\bullet$ ), and IV ( $\bullet$ ); markers highlighted with flow regimes: MSS ( $\color{red}\square$ ), PSS ( $\color{green}\square$ ), HS ( $\color{orange}\square$ ), and CS ( $\color{teal}\square$ ).

emergence of small coherent structures. The  $C_{l,y}-C_{l,z}$  phase diagram shows the variation of the lift direction. We recommend combining these indicators for a more accurate identification. Given the limited data we generated through highly resolved simulations, we provide the critical Reynolds numbers  $Re_{cr}$  with an error bar of  $\pm 5$  in Table I.

#### H. Lift to drag ratio

We plot in Fig. 26 the ratio of the time-averaged  $\overline{C_l}$  over the time-averaged  $\overline{C_d}$  for the five Platonic polyhedrons. To better illustrate the transition, we outline the markers representing the five Platonic polyhedrons with colors corresponding to the flow regimes, as indicated in Table I. In the MSS regime, the vortices generated on the particle surface, with their cores situated in low-pressure regions [56], exhibit multiplanar symmetry and thus equally influence the particle as depicted in Figs. 7 and 8, resulting in a counterbalance of the lateral forces. Consequently,  $\overline{C_l}$  is small and amounts less than 1% of  $\overline{C_d}$  for all Platonic polyhedrons.

The transition from the MSS regime to the PSS regime results in a significant increase in the lift-drag ratio  $\overline{C_l}/\overline{C_d}$ , which corresponds to  $Re_{cr,M \rightarrow P}$  shown in Table I. We underscore the jump of  $\overline{C_l}/\overline{C_d}$  from the MSS regime to the PSS regime with solid lines in Fig. 26. For instance, the CV exhibits a notable increase of  $\overline{C_l}/\overline{C_d}$  between  $Re = 120$  and  $Re = 130$ . In contrast, the jump of  $\overline{C_l}/\overline{C_d}$  in the IV case occurs between  $Re = 200$  and  $Re = 210$ . As the most angular particle, the TV experiences the jump of  $\overline{C_l}/\overline{C_d}$  at a higher  $Re$  than that in the CV and OV cases, between  $Re = 150$  and  $Re = 160$ . Hence,  $Re_{cr,M \rightarrow P}$  corresponding to the significant increase in  $\overline{C_l}/\overline{C_d}$  is not governed by the particle sphericity  $\phi$ , which is consistent with Fig. 6. As illustrated in Fig. 10, the onset of the PSS regime directly results from the merging of vortices with the same sign. In the PSS regime, the similar size of the merged large vortices (illustrated in Fig. 11) maintains a plane of symmetry within the wake vortex pattern, which offsets the lateral forces orthogonal to the symmetry plane. Nonetheless, the difference in the size of the vortices along the direction of the symmetry plane can generate a significant lift force, which results in the jump of  $\overline{C_l}/\overline{C_d}$  in Fig. 26.

In the PSS regime, the OV exhibits a high  $\overline{C_l}/\overline{C_d}$  ratio of approximately 10%. This ratio then sharply decreases in the HS regime before rising again to around 2% in the CS regime. The *V-shape*

evolution of  $\overline{C_l}/\overline{C_d}$  observed between  $Re = 200$  and  $Re = 260$  in the OV case is a consequence of the evolution of the vortex shedding plane state with  $Re$ : unsteady, then stable, and subsequently unsteady again (more details available in Appendix C). When vortices of comparable size are shed in an alternating fashion from the particle wake and the shedding plane is stable, the lift coefficient  $C_l$  exhibits a similar magnitude in two opposite directions centered at 0, resulting in a small time-averaged  $\overline{C_l}$ . Please note that between  $Re = 200$  and  $Re = 260$  in the OV case, the magnitude of the  $C_l$  oscillation stays relatively constant, at approximately  $\pm 0.1$ . Thus, the decrease in the time-averaged  $\overline{C_l}/\overline{C_d}$  is attributed to the existence of a stable shedding plane. We observe similar trends in the TV and CV cases, although the decrease of the magnitude of  $\overline{C_l}/\overline{C_d}$  in the HS regime is not as pronounced as that in the OV case.

For the particles with high angularity (TV, CV, OV), the maximal value of  $\overline{C_l}/\overline{C_d}$  is reached in the PSS regime and remains lower than 10%. In the case of particles of high sphericity (DV, IV),  $\overline{C_l}/\overline{C_d}$  increases to around 10% in the PSS regime and maintains this value at higher  $Re$ . These two particles exhibit higher values of  $\overline{C_l}/\overline{C_d}$  compared to the TV, CV and OV in the unsteady regime. Intriguingly, we observe a phenomenon akin to a *saturation* in the  $\overline{C_l}/\overline{C_d}$  curve in both the DV and IV cases. This phenomenon initiates in the HS regime and persists into the CS regime. A plausible explanation for this could be that the size of the wake recirculation region is bounded by the dimensions of the particle, as portrayed in Figs. 8 and 14. Thus, the difference in size of the vortices produced in the recirculation region would inherently have a limit since they are formed and shed alternately from a wake of finite volume. This limit on the temporal vortex size difference would consequently lead to an upper bound of  $\overline{C_l}/\overline{C_d}$ . For all Platonic polyhedrons,  $\overline{C_l}/\overline{C_d}$  is bounded by a maximal value of 10% in the range of  $100 \leq Re \leq 500$ . Figure 26 underscores that  $\overline{C_l}/\overline{C_d}$  is closely tied to the evolution of the wake vortex structures across various flow regimes.

## VI. DISCUSSION AND PERSPECTIVES

We investigated the regime transitions of an inertial flow past a Platonic polyhedron fixed in an unbounded domain at three different angular positions: an edge, a face and a vertex facing the upcoming flow in the range of Reynolds number  $100 \leq Re \leq 500$ . The key factor of the interaction between the flow and the Platonic polyhedron is the vortex structure generated on the particle surface and in the particle wake, which are pivotal in distinguishing different regimes and governing lateral forces. While we utilize various tools like  $\omega_x$ ,  $\lambda_2$ , and flow velocity streamlines in LIC, their collective purpose is to provide a more detailed portrayal of the vortex structures across differing regimes. Quantitative measures, including  $\overline{C_d}$ ,  $\overline{C_l}/\overline{C_d}$ , phase map of  $C_{l,y} - C_{l,z}$ ,  $f$  and  $St$ , reveal the outcomes of the evolution of vortex structures.

At low Reynolds numbers, the multiplanar symmetry steady (MSS) regime is identified for all Platonic polyhedrons, of which the number of symmetry axis of the vorticity pattern projected in a plane perpendicular to the streamwise direction in the particle wake region is determined by the geometry of the particle front surface. We reveal that the leading edges have a dominant influence on the particle wake structure and symmetry. Each leading edge generates a pair of opposite-signed vortices that are transported by the flow to the wake of the particle while keeping the symmetric properties of the particle front surface. In all flow regimes, the drag force decreases with increasing  $Re$ , but in the MSS regime the lift coefficients are negligible compared to the drag due to the symmetry of the flow structure around and in the wake of the fixed particle. With increasing  $Re$ , the vortices with the same sign merge to form pairs of large vortices in the PSS regime. We show that the merging of the vortices into pairs occurs on the rear faces of the fixed particle, leading to the breakup of the multiplanar symmetry. The symmetry plane in the PSS regime is randomly chosen among the possible symmetry planes of the MSS regime and the lift force starts to increase. As an indicator of the flow symmetry breakup, the total lift coefficient  $\overline{C_l}$  increase with  $Re$  in the PSS regime and have values bounded by 10% of the corresponding drag coefficient  $\overline{C_d}$  in the unsteady flows.

A further increase of  $Re$  leads to unsteady flows, starting with the periodic hairpin vortex shedding (HS, DHS) regime. From the tetrahedron to the icosahedron, the vortex shedding mode varies with the particle sphericity and angular position. In general, the periodic vortex shedding has a Strouhal number of  $S_{St} \approx 0.1 \sim 0.15$ . As a general trend, angularity reduces  $S_{St}$ . For several special particle angular positions such as TE and OE, the shedding frequency can be up to  $S_{St} \approx 0.2$ . We observed and discussed new vortex shedding modes, such as the DHS shedding mode in the TE case and the compact vortex shedding mode in the OE and OF cases. We find that the shape and size of the recirculation region are the key factors that determine the shedding mode and frequency in the HS/DHS regime. A plausible explanation is that particles with a higher aspect ratio of their crosswise cross-sectional surface area tend to have a more flattened recirculation region that results in a higher vortex shedding frequency. Additionally, the shape of the rear surface of the particle influences the recirculation region, thus affecting the shedding mode. With increasing sphericity and as intuitively expected, the shedding mode becomes similar to that in the flow past a fixed sphere, regardless of the particle angular position. In the flow past an edge or face octahedron (OE or OF), we observe single-frequency periodic vortex shedding at a Reynolds number as high as  $Re = 500$ , which indicates that the critical Reynolds number  $Re_{cr}$  of the transition from the HS to the CS regime occurs at  $Re_{cr} > 500$ . In the CS regime, the vortex shedding becomes highly disturbed by the strong flow unsteadiness, but this does not translate into any significant change of the  $\overline{C_l}/\overline{C_d}$  ratio. The dominant shedding frequency  $St$  shifts over time and multiple secondary frequencies arise.

Our study reveals the intrinsic relations between the angular edges and the hairpin vortex generation, clarifies the effects of particle angularity on the flow regime transitions and highlights the crucial role of the flow recirculation region in determining the vortex shedding mode. However, the effects of the particle angularity on the dynamics of the vortex at any angular position remain unclear, as we selected three specific angular positions only. This could be an interesting subject of future investigation. Even with a presumably incomplete data set, the present study does help to depict the general picture of how the angularity of a fixed Platonic polyhedron affects the flow around it. While the increase of the drag coefficient with increasing angularity was intuitively expected, the globally reverse trend of the lift coefficient ( $\overline{C_l}/\overline{C_d}$  decreases with increasing angularity when  $\overline{C_l}/\overline{C_d} > 0.01$ ) is far less intuitive. Eventually, what distinguishes the most a Platonic polyhedron from a sphere is the emergence of nonnegligible transverse forces at much smaller  $Re$ . Setting aside a few specific angular positions, the shedding frequency of Platonic polyhedrons is not significantly different than that of a sphere. We envision two important extensions of the current work before further investigating a fully dynamic suspension of Platonic polyhedrons that we already attempted

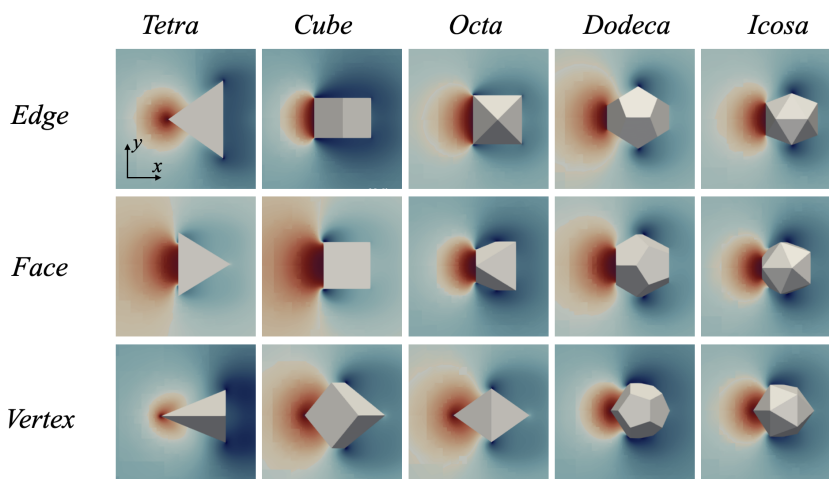


FIG. 27. Pressure distribution colored from min in dark blue to max in dark red in the  $x$ - $y$  plane at  $z = z_p$  around the Platonic polyhedron at different angular positions in the flow at  $Re = 100$ .

in Ref. [20]: (i) pairwise or multibody hydrodynamic interactions in a random array of fixed Platonic polyhedrons and (ii) understanding the Magnus force of Platonic polyhedrons. These two extensions are currently a work in progress and will contribute to complementing the understanding of the effect of angularity in suspensions of isometric angular particles. Platonic polyhedrons, with their well-defined geometric shape, symmetry and duality properties, are perfect toy models to study the effect of angularity in suspension flows in a controlled manner.

### ACKNOWLEDGMENTS

G.G. thanks the Pacific Institute of Mathematical Sciences for their support through his PIMS-CNRS post-doctoral fellowship. The authors greatly appreciate the financial support of the Natural Sciences and Engineering Research Council of Canada (NSERC) via Anthony Wachs New Frontiers in Research Fund grant NFRFE-2018-01922. This research was enabled by support provided by Compute Canada [59] through Anthony Wachs's 2020 and 2021 Computing Resources for Research Groups allocation qpf-764-ac as well as the support provided by the UBC Advanced

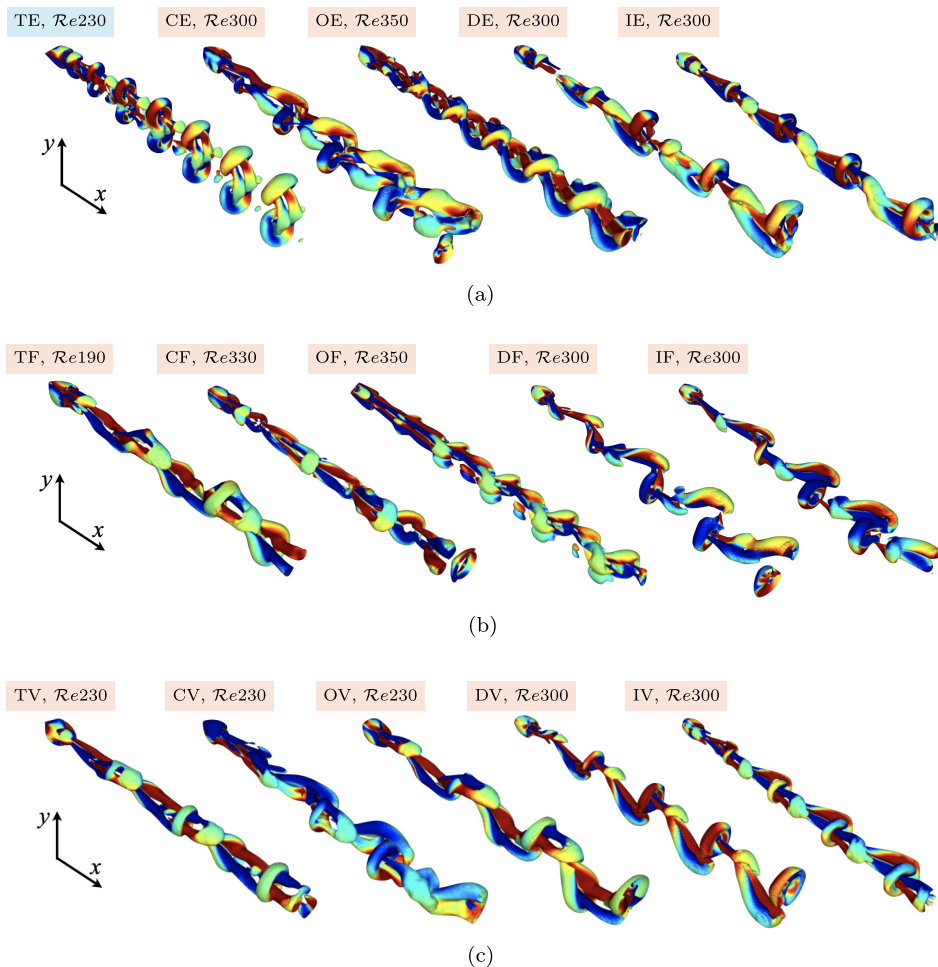


FIG. 28. Three-dimensional view of the wake structures identified by the isosurface of  $\lambda_2 = -1$  and colored by  $u_x$  in the flow past a Platonic polyhedron in the HS/DHS regime. (a) Edge, (b) Face, and (c) Vertex.

Research Computing team through access to the Sockeye supercomputer at the University of British Columbia, Vancouver, Canada.

### APPENDIX A: PRESSURE DISTRIBUTION AROUND A PLATONIC POLYHEDRON IN THE MSS REGIME

Figure 27 shows the pressure distribution of the flow at  $Re = 100$  past a Platonic polyhedron at the three angular positions in the  $x$ - $y$  plane. The pressure distribution around an angular particle depends on its shape and angular position. For example, an edge particle (E) exhibits a local pressure maximum on the leading edge and a decrease in pressure along the side surfaces as the flow is deflected by the front edge. Two pressure minima show up on the rear tips of the TE, the DE, and the IE. The pressure distribution around a face particle (F) exhibits a high-pressure zone on the leading face, with a maximum at the face center. As the fluid leaves the leading face, the pressure drops. In the vertex particle, the pressure remains high as the fluid flows along the front faces of the particle. On the rear surface of the particle, a low-pressure zone appears. The high-pressure distribution around a particle is determined by its front surface. Comparing the tetrahedron at the three angular positions, we see that the TF has a larger high-pressure region than the TE and the TV, which contributes to a higher value of the drag coefficient  $C_d$ . We note that the pressure minima always appear on the particle tips (edges). The shape and size of the low-pressure region behind the particle are closely related to the flow recirculation. As  $\phi$  increases, the pressure distribution becomes more similar to that of a sphere. Knowing how the pressure distribution is affected by the particle angularity, we can better understand the shape of the flow recirculation region and the hairpin vortex formation.

### APPENDIX B: SIDE VIEW OF WAKE STRUCTURES OF A PLATONIC POLYHEDRON IN THE HS REGIME

To provide a more comprehensive illustration of the different hairpin vortex shedding modes, we present three-dimensional view of the vortex structures in Fig. 28. This new perspective

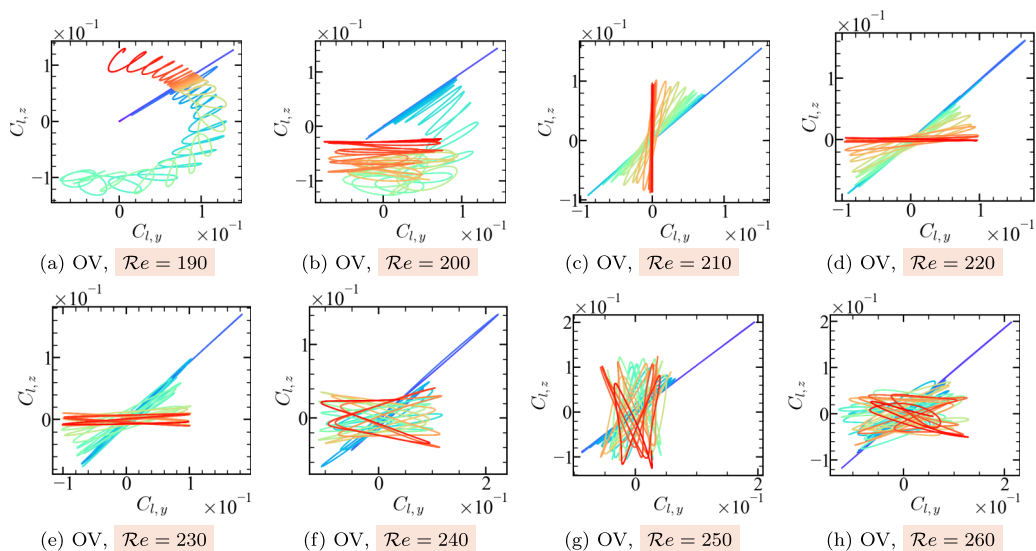


FIG. 29.  $C_{l,y}$ - $C_{l,z}$  phase diagram in the OV case in the HS regime. Time evolution given in rainbow color from purple (start time) to red (end time).

complements and expands upon the information shown in Fig. 12, offering a clearer understanding of both the vortex shedding mode and frequency.

### APPENDIX C: ROTATING STABLE VORTEX SHEDDING PLANE

The evolution of the  $C_{l,y}$ - $C_{l,z}$  phase diagram in the OV case at  $190 \leq \text{Re} \leq 260$  is depicted in Fig. 29. The phase diagram reveals stable behavior of the vortex shedding plane on a short timescale and a slow rotation on a large timescale at  $210 \leq \text{Re} \leq 230$ . As Re increases, the stability of the rotating shedding plane on a short timescale becomes compromised. The frequent appearance of rotating stable shedding planes at vertex angular positions such as TV, OV, and DV cases is primarily due to the challenges in maintaining a steady shedding plane when flow streams converge from multiple directions. For example, in the OV case, three flow streams merge at the rear vertex. The wake structures continuously seek the *stable* plane among the multiple symmetry planes in the MSS regime.

- 
- [1] R. Williams and M. Follows, *Ocean Dynamics and the Carbon Cycle: Principles and Mechanisms* (Cambridge University Press, Cambridge, UK, 2011)
  - [2] F. Auguste and J. Magnaudet, Path oscillations and enhanced drag of light rising spheres, *J. Fluid Mech.* **841**, 228 (2018).
  - [3] G. Gai, S. Kudriakov, B. Rogg, A. Hadjadj, E. Studer, and O. Thomine, Numerical study on laminar flame velocity of hydrogen-air combustion under water spray effects, *Int. J. Hydrog. Energy* **44**, 17015 (2019).
  - [4] D. Bi, T. Sun, Y. Wei, and X. Huang, On the dynamic behaviors of freely falling annular disks at different Reynolds numbers, *Phys. Fluids* **34**, 043307 (2022).
  - [5] G. Mougine and J. Magnaudet, The generalized Kirchhoff equations and their application to the interaction between a rigid body and an arbitrary time-dependent viscous flow, *Int. J. Multiph. Flow* **28**, 1837 (2002).
  - [6] A. Seyed-Ahmadi and A. Wachs, Sedimentation of inertial monodisperse suspensions of cubes and spheres, *Phys. Rev. Fluids* **6**, 044306 (2021).
  - [7] H. Jiang and L. Cheng, Flow separation around a square cylinder at low to moderate Reynolds numbers, *Phys. Fluids* **32**, 044103 (2020).
  - [8] P. Ern, F. Risso, P. C. Fernandes, and J. Magnaudet, Dynamical Model for the Buoyancy-Driven Zigzag Motion of Oblate Bodies, *Phys. Rev. Lett.* **102**, 134505 (2009).
  - [9] V. Mathai, X. Zhu, C. Sun, and D. Lohse, Mass and Moment of Inertia Govern the Transition in the Dynamics and Wakes of Freely Rising and Falling Cylinders, *Phys. Rev. Lett.* **119**, 054501 (2017).
  - [10] S. Gao, L. Tao, X. Tian, and J. Yang, Flow around an inclined circular disk, *J. Fluid Mech.* **851**, 687 (2018).
  - [11] L. Schneiders, K. Fröhlich, M. Meinke, and W. Schröder, The decay of isotropic turbulence carrying nonspherical finite-size particles, *J. Fluid Mech.* **875**, 520 (2019).
  - [12] S. Taneda, Experimental investigation of the wake behind a sphere at low Reynolds numbers, *J. Phys. Soc. Jpn.* **11**, 1104 (1956).
  - [13] I. Nakamura, Steady wake behind a sphere, *Phys. Fluids* **19**, 5 (1976).
  - [14] M. Kiya, H. Ishikawa, and H. Sakamoto, Near-wake instabilities and vortex structures of three-dimensional bluff bodies: A review, *J. Wind Eng. Ind. Aerodyn.* **89**, 1219 (2001).
  - [15] F. Cocetta, M. Gillard, J. Szmelter, and P. K. Smolarkiewicz, Stratified flow past a sphere at moderate Reynolds numbers, *Comput. Fluids* **226**, 104998 (2021).
  - [16] R. Magarvey and R. Bishop, Transition ranges for three-dimensional wakes, *Can. J. Phys.* **39**, 1418 (1961).
  - [17] T. Johnson and V. Patel, Flow past a sphere up to a Reynolds number of 300, *J. Fluid Mech.* **378**, 19 (1999).
  - [18] A. Saha, Three-dimensional numerical simulations of the transition of flow past a cube, *Phys. Fluids* **16**, 1630 (2004).

- [19] M. Rahmani and A. Wachs, Free falling and rising of spherical and angular particles, *Phys. Fluids* **26**, 083301 (2014).
- [20] A. Seyed-Ahmadi and A. Wachs, Dynamics and wakes of freely settling and rising cubes, *Phys. Rev. Fluids* **4**, 074304 (2019).
- [21] M. Khan, A. Sharma, and A. Agrawal, Simulation of flow around a cube at moderate Reynolds numbers using the lattice Boltzmann method, *J. Fluids Eng.* **142**, 011301 (2019).
- [22] F. Y. Fraige, P. A. Langston, and G. Z. Chen, Distinct element modelling of cubic particle packing and flow, *Powder Technol.* **186**, 224 (2008).
- [23] A. Saha, Three-dimensional numerical study of flow and heat transfer from a cube placed in a uniform flow, *Int. J. Heat Fluid Flow* **27**, 80 (2006).
- [24] L. Klotz, S. Goujon-Durand, J. Rokicki, and J. Wesfreid, Experimental investigation of flow behind a cube for moderate Reynolds numbers, *J. Fluid Mech.* **750**, 73 (2014).
- [25] G. Gai and A. Wachs, High fidelity adaptive Cartesian octree grid computations of the flow past a Platonic polyhedron up to a Reynolds number of 200, *Powder Technol.* **420**, 118390 (2023).
- [26] Q. Meng, H. An, L. Cheng, and M. Kimiaei, Wake transitions behind a cube at low and moderate Reynolds numbers, *J. Fluid Mech.* **919**, A44 (2021).
- [27] J. T. Stuart, On the nonlinear mechanics of wave disturbances in stable and unstable parallel flows Part 1. The basic behaviour in plane Poiseuille flow, *J. Fluid Mech.* **9**, 353 (1960).
- [28] S. Whitaker, Forced convection heat transfer correlations for flow in pipes, past flat plates, single cylinders, single spheres, and for flow in packed beds and tube bundles, *AIChE J.* **18**, 361 (1972).
- [29] J. Gabitto and C. Tsouris, Drag coefficient and settling velocity for particles of cylindrical shape, *Powder Technol.* **183**, 314 (2008).
- [30] L. Cheng, X. Ju, F. Tong, and H. An, Transition to chaos through period doublings of a forced oscillating cylinder in steady current, *J. Fluid Mech.* **887**, A5 (2020).
- [31] E. Loth, Drag of nonspherical solid particles of regular and irregular shape, *Powder Technol.* **182**, 342 (2008).
- [32] A. Richter and P. Nikrityuk, Drag forces and heat transfer coefficients for spherical, cuboidal and ellipsoidal particles in cross flow at subcritical Reynolds numbers, *Int. J. Heat Mass Transf.* **55**, 1343 (2012).
- [33] P. Bohorquez, E. Sanmiguel-Rojas, A. Sevilla, J. I. Jiménez-González, and C. Martínez-Bazán, Stability and dynamics of the laminar wake past a slender blunt-based axisymmetric body, *J. Fluid Mech.* **676**, 110 (2011).
- [34] H. Yow, M. Pitt, and A. Salman, Drag correlations for particles of regular shape, *Adv. Powder Technol.* **16**, 363 (2005).
- [35] E. Pettyjohn and E. Christiansen, Effect of particle shape on free settling rates of isometric particles., *Chem. Eng. Prog.* **44**, 157 (1948).
- [36] A. Haider and O. Levenspiel, Drag coefficient and terminal velocity of spherical and nonspherical particles, *Powder Technol.* **58**, 63 (1989).
- [37] D. Leith, Drag on nonspherical objects, *Aerosol Sci. Technol.* **6**, 153 (1987).
- [38] G. Ganser, A rational approach to drag prediction of spherical and nonspherical particles, *Powder Technol.* **77**, 143 (1993).
- [39] K. Wittig, A. Richter, and P. Nikrityuk, Numerical study of heat and fluid flow past a cubical particle at subcritical Reynolds numbers, *Comp. Thermal Sciences* **4**, 283 (2012).
- [40] A. Hölzer and M. Sommerfeld, New simple correlation formula for the drag coefficient of nonspherical particles, *Powder Technol.* **184**, 361 (2008).
- [41] A. Hölzer and M. Sommerfeld, Lattice Boltzmann simulations to determine drag, lift and torque acting on nonspherical particles, *Comput. Fluids* **38**, 572 (2009).
- [42] J. McNown and J. Malaika, Effects of particle shape on settling velocity at low Reynolds numbers, *Trans. A.G.U.* **31**, 74 (1950).
- [43] G. Gai and A. Wachs, Dynamics, wakes, and regime transitions of a fixed angular particle in an unbounded inertial flow. I. Regular tetrahedron angular position, *Phys. Rev. Fluids* **8**, 064304 (2023).

- [44] P. Ern, F. Risso, D. Fabre, and J. Magnaudet, Wake-induced oscillatory paths of bodies freely rising or falling in fluids, *Annu. Rev. Fluid Mech.* **44**, 97 (2012).
- [45] J. Lin and H. Chen, Lattice Boltzmann simulation of fluid flow through random packing beds of Platonic particles: Effect of particle characteristics, *Particuology* **47**, 41 (2019).
- [46] H. Zhang, X. Bo, X. An, C. Ke, and J. Chen, Numerical prediction on the drag force and heat transfer of nonspherical particles in supercritical water, *Powder Technol.* **361**, 414 (2020).
- [47] R. Glowinski, T. Pan, T. Hesla, and D. Joseph, A distributed Lagrange multiplier/fictitious domain method for particulate flows, *Int. J. Multiph. Flow* **25**, 755 (1999).
- [48] A. Wachs, A DEM-DLM/FD method for direct numerical simulation of particulate flows: Sedimentation of polygonal isometric particles in a Newtonian fluid with collisions, *Comput. Fluids* **38**, 1608 (2009).
- [49] A. Wachs, PeliGRIFF, A parallel DEM-DLM/FD direct numerical simulation tool for 3D particulate flows, *J. Eng. Math.* **71**, 131 (2011).
- [50] A. Wachs, A. Hammouti, G. Vinay, and M. Rahmani, Accuracy of finite volume/staggered grid distributed Lagrange multiplier/fictitious domain simulations of particulate flows, *Comput. Fluids* **115**, 154 (2015).
- [51] C. Selçuk, A. R. Ghigo, S. Popinet, and A. Wachs, A fictitious domain method with distributed Lagrange multipliers on adaptive quad/octrees for the direct numerical simulation of particle-laden flows, *J. Comput. Phys.* **430**, 109954 (2021).
- [52] S. Popinet, A quadtree-adaptive multigrid solver for the Serre–Green–Naghdi equations, *J. Comput. Phys.* **302**, 336 (2015).
- [53] A. D. Rakotonirina, J.-Y. Delenne, F. Radjai, and A. Wachs, Grains3D, a flexible DEM approach for particles of arbitrary convex shape—Part III: Extension to nonconvex particles modelled as glued convex particles, *Comput. Part. Mech.* **6**, 55 (2019).
- [54] A. Wachs, L. Girolami, G. Vinay, and G. Ferrer, Grains3D, a flexible DEM approach for particles of arbitrary convex shape—Part I: Numerical model and validations, *Powder Technol.* **224**, 374 (2012).
- [55] A. Seyyed-Ahmadi and A. Wachs, Microstructure-informed probability-driven point-particle model for hydrodynamic forces and torques in particle-laden flows, *J. Fluid Mech.* **900**, A21 (2020).
- [56] J. Jeong and F. Hussain, On the identification of a vortex, *J. Fluid Mech.* **285**, 69 (1995).
- [57] Z. Yu, N. Phan-Thien, Y. Fan, and R. Tanner, Viscoelastic mobility problem of a system of particles, *J. Non-Newton. Fluid Mech.* **104**, 87 (2002).
- [58] A. A. Johnson and T. E. Tezduyar, Advanced mesh generation and update methods for 3D flow simulations, *Comput. Mech.* **23**, 130 (1999).
- [59] <https://alliancecan.ca/en>.